TECTONICS, VOL. 32, 1454–1479, doi:10.1002/tect.20086, 2013

Evidence for constriction and Pliocene acceleration of east-west extension in the North Lunggar rift region of west central Tibet

Kurt E. Sundell,[1] Michael H. Taylor,[1] Richard H. Styron,[1,2] Daniel F. Stockli,[1,3] Paul Kapp,[4] Christian Hager,[1,5] Deliang Liu,[6] and Lin Ding[6]

Received 17 March 2013; revised 29 August 2013; accepted 12 September 2013; published 10 October 2013.

[1] The active north trending North Lunggar rift in west central southern Tibet exposes an extensional metamorphic core complex bounded by an east dipping low-angle normal fault. Apatite and zircon (U-Th)/He thermochronology and thermal modeling of the North Lunggar rift document a minimum timing for rift inception at >10 Ma and rapid footwall exhumation between 5 and 2 Ma. Miocene footwall cooling and exhumation rates were initially slow to moderate at <50°C Ma^{-1} and <1 mm a^{-1}, followed by increased Pliocene rates as high as >400°C Ma^{-1} and 4–10 mm a^{-1}. Footwall isotherms were significantly compressed during rapid exhumation resulting in an elevated transient geothermal gradient between 50 and 90°C km^{-1}. The minimum magnitude of horizontal extension for the North Lunggar rift is 8.1–12.8 km; maximum is 15–20 km, less in the south at ~10 km. Mean Pliocene extension rate is 1.2–2.4 mm a^{-1} in the ~120° direction. Results for the North Lunggar rift are similar in magnitude, rate, and orientation of slip to the kinematically linked Lamu Co dextral strike-slip fault to the north. This suggests a state of constrictional strain during Pliocene time along this stretch of the Bangong-Nujiang suture from which the Lamu Co fault emanates. The onset of extension in this region may be explained by crustal thickening and gravitational orogenic collapse, followed by accelerated rifting resulting from localized crustal stretching and increased magmatic activity, potentially driven by the position and northward extent of underthrusting Indian lithosphere.

Citation: Sundell, K. E., M. H. Taylor, R. H. Styron, D. F. Stockli, P. Kapp, C. Hager, D. Liu, and L. Ding (2013), Evidence for constriction and Pliocene acceleration of east-west extension in the North Lunggar rift region of west central Tibet, *Tectonics*, *32*, 1454–1479, doi:10.1002/tect.20086.

1. Introduction

[2] The Himalayan-Tibetan orogen is the largest active contractional orogen on Earth. It was produced by the sequential accretion of multiple terranes to the southern margin of Eurasia and the collision and northward underthrusting of India beneath Asia [*Allégre et al*., 1984; *Yin and Harrison*, 2000]. Despite ongoing north-south convergence, active deformation in southern and central Tibet is characterized by east-west extension, with the majority of active shortening limited to the outermost margins of the plateau [*Taylor and Yin*, 2009; *Styron et al.*, 2010] (Figure 1). Syncollisional extension has been ascribed to processes involving continuum deformation driven by orogenic collapse [*Dewey*, 1988]; delamination of thickened mantle lithosphere [*England and Houseman*, 1988, 1989]; eastward extrusion of Tibetan lithosphere driven by east directed flow of a low-viscosity middle crust [*Nelson et al*., 1996], lower crust [*Royden*, 1996; *Royden et al*., 1997; *Clark and Royden*, 2000; *Huang et al*., 2000], or asthenosphere [*Yin and Taylor*, 2011]; oblique collision [*McCaffery and Nábělek*, 1998]; northward underthrusting of the Indian slab [*DeCelles et al*., 2002; *Liu and Yang*, 2003; *Kapp and Guynn*, 2004; *Copley et al*., 2011]; oroclinal bending [*Klootwijk et al*., 1985; *Schill et al*., 2001; *Li and Yin*, 2008]; or far-field effects driven by rollback of the Pacific oceanic plate [*Dewey*, 1980; *Yin*, 2000].

[3] Active extension within Tibet's interior is expressed as an array of kinematically linked north trending rifts and V-shaped conjugate strike-slip fault systems along the Bangong-Nujiang suture zone (BNS) (Figure 1) [*Taylor*

Additional supporting information may be found in the online version of this article.

[1]Department of Geology, University of Kansas, Lawrence, Kansas, USA.
[2]Now at Earth and Environmental Sciences, University of Michigan, Ann Arbor, Michigan, USA.
[3]Now at the Department of Geological Sciences, University of Texas at Austin, Austin, Texas, USA.
[4]Department of Geosciences, University of Arizona, Tucson, Arizona, USA.
[5]Now at Chevron U.S.A. Inc., Bakersfield, California, USA.
[6]Institute of Tibetan Plateau Research, Chinese Academy of Sciences, Beijing, China.

Corresponding author: K. E. Sundell, Department of Earth and Atmospheric Sciences, University of Houston, 312 Science and Research Building 1, Rm. 312, Houston, TX 77204-5007, USA. (kesundell@uh.edu)

0278-7407/13/10.1002/tect.20086

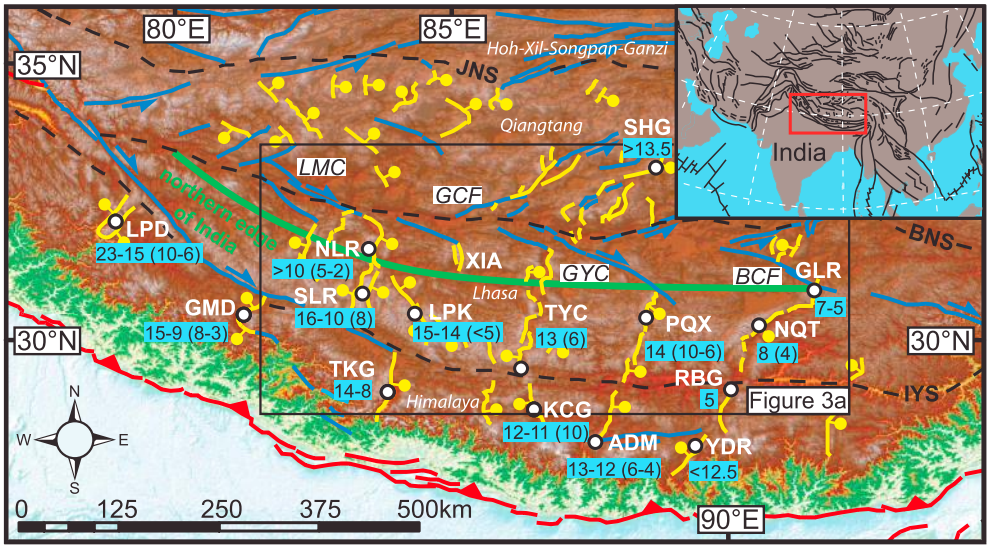

Figure 1. Color-shaded relief map of the Himalayan-Tibetan orogen. Digital elevation model generated from the Shuttle Radar Topography Mission 90 m elevation data. Active contractional (barbs on upper plate), extensional (bar and ball on hanging wall) and strike-slip (arrows indicate direction of horizontal motion) structures, and inactive sutures (dashed black lines) after *Styron et al.* [2010]. BNS = Bangong-Nujiang suture. IYS = Indus-Yarlung suture. JNS = Jinsha suture. Qilian and Kunlun terranes (not shown) are located to the north of the Hoh-Xil-Songpan-Ganzi terrane. Light blue boxes = estimates for the onset of east-west extension (numbers in parentheses indicate timing of accelerated footwall exhumation). Green line represents the northern extent of subducted Indian crust [*Nábělek et al.*, 2009]. ADM = Ama Drime massif [*Kali et al.*, 2010]. GLR = Gulu rift [*Stockli et al.*, 2002a]. GMD = Gurla Mandhata dome [*Murphy et al.*, 2002; McCallister et al., submitted manuscript, 2013]. KCG = Kung Co graben [*Lee et al.*, 2011]. LPK = Lopukangri [*Murphy et al.*, 2010; *Sanchez et al.*, 2010]. LPD = Leo Pargil dome [*Thiede et al.*, 2006; *Langille et al.*, 2012]. NLR = North Lunggar rift [*Kapp et al.*, 2008; this study]. NQT = Nyainqentanghla Shan [*Harrison et al.*, 1995; *J. Kapp et al.*, 2005]. PQX = Pum Qu-Xainza rift [*Hager et al.*, 2009]. RBG = Ringbung graben [*Ratschbacher et al.*, 2011]. SHG = Shuang Hu graben [*Blisniuk et al.*, 2001]. SLR = South Lunggar rift [*Styron et al.*, 2013]. TKG = Thakkhola graben [*Garzione et al.*, 2000]. TYC = Tangra Yum Co [*Dewane et al.*, 2006]. YDR = Yadong rift [*Edwards and Harrison*, 1997]. Inset fault map after *Yin* [2010].

and Yin, 2009; *Yin and Taylor*, 2011]. This deformation style is suggestive of constrictional strain. Simple constriction is characterized by uniform extension in one direction with roughly equal shortening in all directions at right angles to it ($\hat{s}_1 > 1 > \hat{s}_2 = \hat{s}_3$; $\hat{s}$ refers to principal stretch where $\hat{s} > 1$ is lengthening and $\hat{s} < 1$ is shortening), resulting in a cigar-shaped, prolate strain ellipsoid [*Twiss and Moores*, 2007] (Figure 2). Central Tibetan deformation is more characteristic of general constriction (herein referred to simply as constriction), meaning $\hat{s}_2$ and $\hat{s}_3$ need not be equal ($\hat{s}_1 > 1 > \hat{s}_2 > \hat{s}_3$). Local stress states will differ in purely strike-slip (σ_2 vertical) and purely dip-slip (σ_1 vertical) fault regimes but together can result in a regionally constrictional strain field, with surface deformation manifest as a network of strike-slip and dip-slip faults (Figure 2). In central and southern Tibet, active kinematically linked strike-slip and normal fault pairs exhibit similar orientations of fault slip vectors consistent with eastward motion of central Tibet [*Mercier et al.*, 1987; *Taylor et al.*, 2003; *Yin and Taylor*, 2011], with the regional maximum principal stretching direction ($\hat{s}_1$) oriented approximately east-west [*Zhang et al.*, 2004]. Assuming the magnitude of vertical thinning is less than the magnitude of north-south contraction

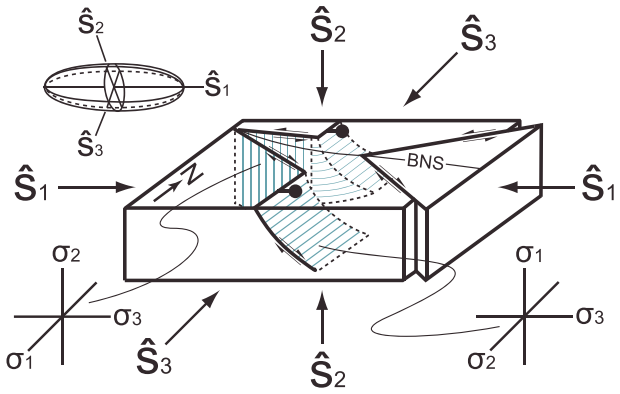

Figure 2. General constriction ($\hat{s}_1 > 1 > \hat{s}_2 > \hat{s}_3$) as described by a prolate (cigar-shaped) strain ellipsoid (upper left) ($\hat{s}$ = principal stretch; $\hat{s} > 1$ = lengthening and $\hat{s} < 1$ = shortening) [*Twiss and Moores*, 2007], as applied to central Tibetan deformation resulting from stress states characterized by extensional (σ_1 vertical) and strike-slip (σ_2 vertical) structures. BNS = Bangong-Nujiang suture.

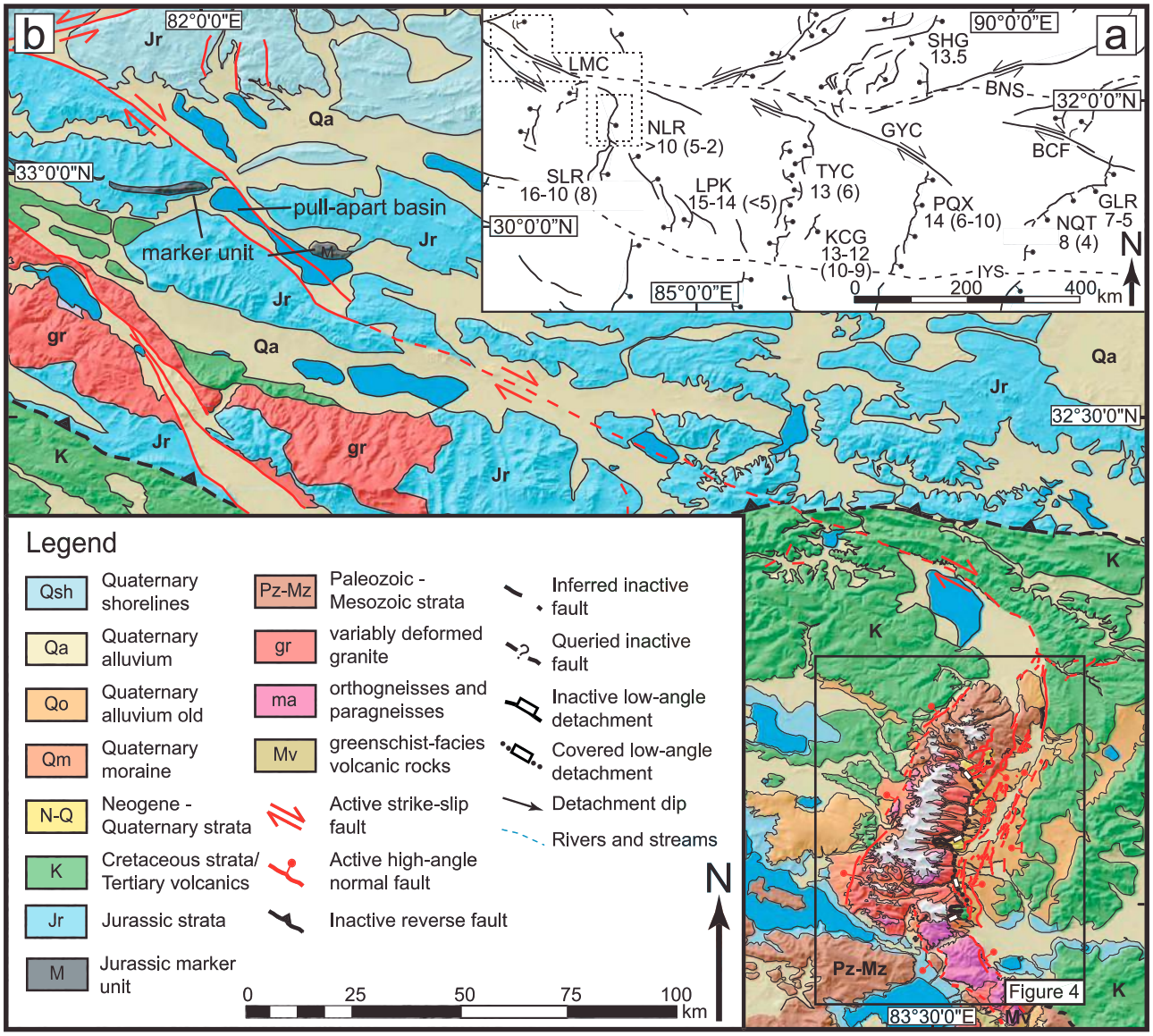

Figure 3. (a) Active structures in southern Tibet after *Styron et al.* [2010] (see Figure 1 for references). (b) Geologic map of the Lamu Co dextral strike-slip fault (modified from *Taylor et al.* [2003]) and its kinematic linkage to the North Lunggar rift (modified from *Kapp et al.* [2008]). Digital elevation models generated from the Shuttle Radar Topography Mission 90 m elevation data.

implies a vertically oriented intermediate stretching direction ($\hat{s}_2$) and a minimum stretching direction oriented north-south ($\hat{s}_3$). This inference is consistent with the surface expression of active structures based on field observations of Quaternary normal and strike-slip faults [*Armijo et al.*, 1986, 1989; *Taylor et al.*, 2003] and earthquake moment tensor analysis which show strike-slip and normal fault activity throughout Tibet [e.g., *Molnar and Lyon-Caen*, 1989]. Constrictional strain is also supported by the observed increase in the eastward component of the GPS velocity field along the BNS [*Zhang et al.*, 2004] as well as high rates of strike-slip faulting along both sinistral and dextral faults north and south of the BNS, as shown by synthetic aperture radar interferometry (InSAR) [*Taylor and Peltzer*, 2006].

[4] Timing constraints for active structures are necessary to assess models attempting to explain the development of the Himalayan-Tibetan orogen. Estimates are, however, limited, as there are few data constraining the initiation of extension directly and even fewer constraints on the initiation age and slip-rate histories of strike-slip faults within the orogen. Estimates for the onset of extension vary from the early [e.g., *Williams et al.*, 2001; *Gao et al.*, 2007] to middle-late Miocene [e.g., *Coleman and Hodges*, 1995; *Harrison et al.*, 1995; *Blisniuk et al.*, 2001], with many estimates showing evidence for more recent episodes of accelerated late Miocene-Pliocene exhumation [*Stockli et al.*, 2002a; *Dewane et al.*, 2006; *Hager et al.*, 2009; *Sanchez et al.*, 2010; *Styron et al.*, 2013; this study] (Figure 1). The initiation age of strike-slip faults along the BNS is essentially unknown; however, it has

been hypothesized that they formed in Pliocene time [e.g., *Armijo et al*., 1989; *Taylor and Peltzer*, 2006]. If strain in central Tibet is indeed characterized by constriction, then the kinematically linked strike-slip and normal faults should exhibit comparable ages of fault initiation and magnitudes of fault slip, as well as slip rate. One hypothesis is that normal-strike-slip structure pairs should exhibit the same age for initiation across Tibet, suggesting there is constrictional deformation across Tibet [e.g., *Mercier et al*., 1987], whereas another suggests spatially diachronous initiation of faulting with younger structure pairs to the west [*Yin and Taylor*, 2011].

[5] This study constrains the timing, rate, and magnitude of extension for the North Lunggar rift—a large-magnitude (> 10 km extension in its central part), active, north trending rift bounded by high- and low-angle normal faults in western Tibet (Figures 3 and 4) [*Kapp et al*., 2008]. The North Lunggar rift displays an apparent kinematic linkage to the Lamu Co dextral strike-slip fault to the north, which together represent the westernmost documented example of a normal-strike-slip fault pair in central Tibet. We present new apatite and zircon (U-Th)/He thermochronological data and zircon U-Pb geochronological data from the North Lunggar rift. Thermal modeling constrains plausible time-temperature (t-T) cooling histories for the North Lunggar rift footwall and associated geothermal gradients during rift activity. Characterization of the thermal history and thermal structure of this Tibetan rift has implications for the development of large-magnitude extension in areas of actively, or formerly active, extending regions of hot, thickened crust capable of ductile flow at midcrustal levels. Furthermore, constraining the rate, magnitude, and orientation of extension for this rift provides an opportunity for comparison to the apparently kinematically linked Lamu Co dextral strike-slip fault system to the north. Our results have implications for the interaction between strike-slip faults and north trending rift systems, the recent orientation of the strain field in central Tibet, and to models explaining how ongoing India-Asia convergence is accommodated within the plateau interior.

2. Geologic Background

[6] The Tibetan plateau is the largest and highest plateau on Earth, covering an area approximately 3500 by 1500 km with a mean elevation of ~5000 m [*Fielding et al*., 1994]. The geologic history of the Tibetan plateau involves the accretion of several microcontinents, flysch complexes, and island arc systems to the southern margin of Eurasia commencing in early Paleozoic time with the closure of the Paleo-Tethys ocean between Laurasia in the north and Gondwana to the south [*Allégre et al*., 1984; *Dewey et al*., 1988; *Yin and Harrison*, 2000]. The Indian-affinity Tethyan Himalaya collided with the southern margin of Asia at or by 52–50 Ma [*Garzanti et al*., 1987; *Zhu et al*., 2005; *Green et al*., 2008; *Wang et al*., 2011]. Since then, ~3000 km of convergence as been accommodated between stable India and Eurasia [e.g., *van Hinsbergen et al*., 2011].

[7] The interior of the plateau consists of four terranes between two mountain belts. From north to south these terranes are the Hoh-Xil-Songpan-Ganzi, Qiangtang, Lhasa, and Tethyan Himalayan terranes that lie between the Kunlun Shan in the north and the Himalaya to the south [*Yin and Harrison*, 2000] (Figure 1). The Songpan-Ganzi terrane accreted to the Kunlun Shan along the Anyimaqen-Kunlun-Muztagh suture zone in Paleozoic time [*Yin and Harrison*, 2000], followed by the Qiangtang terrane accreting to the Songpan-Ganzi terrane along the Jinsha suture (JNS) in the Triassic to Early Jurassic, and the Lhasa terrane to the south in the early Cretaceous [*Dewey et al*., 1988; *Yin and Harrison*, 2000; *Kapp et al*., 2003, 2007].

[8] Crustal shortening and contraction at the surface along the BNS and the Indus-Yarlung suture zone (IYS) were active until ~20 Ma [*Kapp et al*., 2007]; however, deformation within the Lhasa block itself was minimal throughout the Cenozoic based on the relatively flat-lying Paleogene Linzizong volcanic sequence and associated youngest phases of Gangdese plutons that form an east-west linear belt along its southern margin [*Yin and Harrison*, 2000]. Shortening along Tibet's southern boundary and the successive development of the Great Counter thrust system, the Main Central thrust, and Main Boundary thrust show a southward propagation of contractional deformation in early Miocene time that immediately preceded the onset of extension in southern Tibet [*Yin et al*., 1994; *Hubbard and Harrison*, 1989; *DeCelles et al*., 2002, 2011]. Extension and strike-slip faulting in the Himalaya commenced in middle Miocene [e.g., *Murphy and Copeland*, 2005; *Thiede et al*., 2006] to late Miocene-Pliocene [e.g., *Edwards and Harrison*, 1997; *Li and Yin*, 2008; *Lee et al*., 2011] time.

[9] Today, the majority of shortening is limited to the outer rims of the Tibetan plateau, expressed as range-parallel fold-and-thrust belts in the Himalaya to the south, and the Qimen Tagh-Kunlun Shan and Qilian Shan along the northeastern boundary [*Taylor and Yin*, 2009]. The northern plateau is characterized by active sinistral strike-slip faulting along the Altyn Tagh fault and active contraction and uplift within the eastern Kunlun Shan, Qaidam Basin, and Qilian Shan-Nan Shan [*Yin and Harrison*, 2000].

2.1. Extensional and Strike-Slip Structures in Central and Southern Tibet

[10] Normal and strike-slip faults in central and southern Tibet cut and offset the preexisting east-west trending Mesozoic-Tertiary fold-thrust belt structural grain [*Armijo et al*., 1986, 1989; *Taylor et al*., 2003; *Kapp et al*., 2007; *Yin and Taylor*, 2011]. Southern Tibetan rifts generally have a stronger morphological expression than central Tibetan rifts [*Fielding et al*., 1994], potentially due to strike-slip faulting being more dominant in central Tibet where rifts typically occur as left step overs in sinistral strike-slip fault systems [*Blisniuk et al*., 2001; *Taylor et al*., 2003]. Rift spacing is variable in central Tibet and regular in southern Tibet [*Armijo et al*., 1986; *Yin*, 2000]. North trending rifts in southern Tibet are characterized by relatively short wavelength (30–40 km) narrow rift flank uplifts [*Masek et al*., 1994], the more evolved of which show evidence for doming of the footwalls of normal faults, and associated topographic highs within the rift valleys [*Harrison et al*., 1995; *J. Kapp et al*., 2005; *Kapp et al*., 2008; *Styron et al*., 2013; this study]. These more developed extensional domains in southern Tibet (Nyainqentanghla and Lunggar rifts) are bound by low-angle (30–40°) normal faults that juxtapose ductilely deformed midcrustal rocks in their footwalls against low-grade, upper crustal rocks in the hanging walls and rift valleys [*J. Kapp et al*., 2005; *Kapp et al*., 2008; *Styron et al*., 2013; this study].

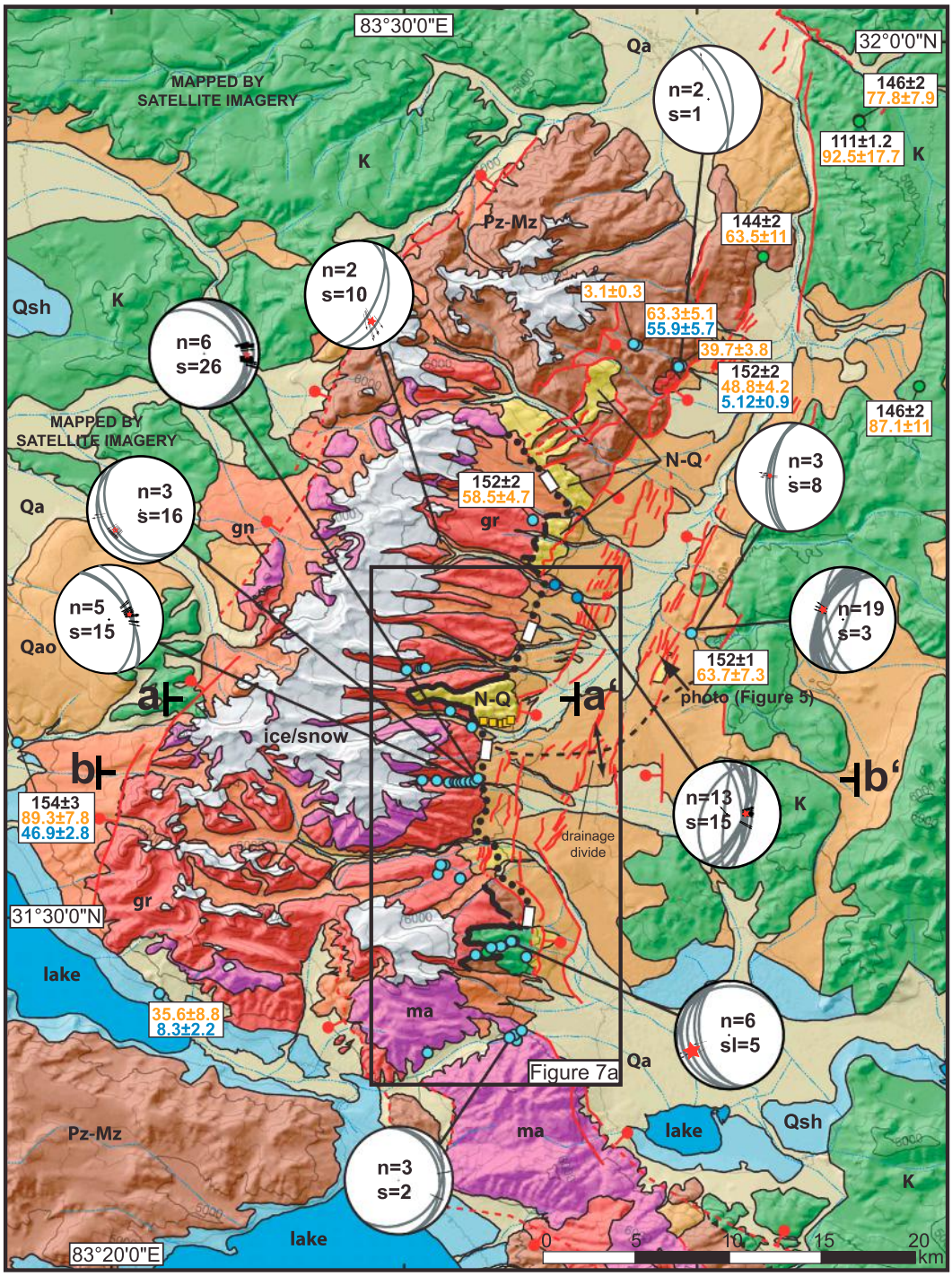

Figure 4. Geologic map of the North Lunggar rift (modified from *Kapp et al*. [2008]). Light blue circles = bedrock apatite (blue text) and zircon (orange text) (U-Th)/He, and zircon U-Pb (black text) sample locations. Dark blue circles = detrital zircon (U-Th)/He ages. Orange squares = detrital samples from *Woodruff et al*. [2013]. Map units and symbols are the same as those in Figure 3. Digital elevation models generated from the Shuttle Radar Topography Mission 90 m elevation data. Fault plane orientations, striations, foliations, and lineations were analyzed using lower hemisphere equal area stereonets (plotted with Stereonet 9 v. 6.3.3 by Richard Allmendinger). Foliation and fault plane striation and lineation data exhibit east-west extension accommodated on both high- and low-angle structures and top-to-the-east shear sense in the footwall. Red stars represent mean slip vector; size of star represents the 95% confidence interval.

[11] Extension in central and southern Tibet commenced in Miocene time; however, precise timing constraints for extensional structures are limited [e.g., *Harrison et al*., 1995; *Blisniuk et al*., 2001]. Evidence for east-west extension signifying a changing stress regime during the middle Miocene may be recorded by the emplacement of north trending dikes across the plateau that yield $^{40}Ar/^{39}Ar$ ages between 18 and 13 Ma [*Yin et al*., 1994; *Williams et al*., 2001], although these are not seen as widespread features associated with Tibetan rift development because their emplacement and formation does not require the maximum principal stress (σ_1) to be vertical to emplace such dikes [*Mahéo et al*., 2007; *Lee et al*., 2011].

[12] Strike-slip faults, despite their early recognition [*Molnar and Tapponnier*, 1975, 1978] and field-based documentation [*Armijo et al*., 1989; *Taylor et al*., 2003], similarly have sparse timing constraints. Conjugate strike-slip faults along the BNS may have formed as recently as Pliocene time, based on reconstructions using mapped geologic offsets and modern slip rates derived from InSAR analysis [*Taylor and Peltzer*, 2006], although the uncertainties are large. Regional compilation and analysis of active structures suggests strike-slip faulting, and the current neotectonic regime in central Tibet began between 6 and 4 Ma [*Ratschbacher et al*., 2011].

[13] There are four major north and northeast trending rift systems in southern Tibet with apparent kinematic linkages to conjugate strike-slip faults along the BNS. From east to west these are the Yadong-Gulu, Pum Qu-Xainza, Tangra Yum Co, and Lunggar rifts (Figures 1 and 3a). The ~N30°E striking Yadong-Gulu rift is approximately 470 km in length along strike, stretches across southern Tibet into the Himalaya, crosscutting both the BNS and IYS, and is the most extensively documented Tibetan rift [*Armijo et al*., 1986, 1989; *Burchfiel et al*., 1991; *Pan and Kidd*, 1992; *Harrison et al*., 1995; *J. Kapp et al*., 2005]. The central portion of the Yadong-Gulu rift (Nyainqentanghla Shan) appears to be the most well-developed and most topographically expressed rift in southern Tibet, exhuming high-grade metamorphic rocks and mylonites in its footwall, with an initiation age of 8 ± 1 Ma [*Harrison et al*., 1995; *J. Kapp et al*., 2005]. To the north, apatite (U-Th)/He ages from the Gulu segment document rapid exhumation and cooling between 7 and 5 Ma [*Stockli et al*., 2002a]. Cumulative east-west extension estimates for the Yadong-Gulu rift are between 14 and 26 km for the Nyainqentanghla Shan, with higher slip estimates assuming that extension is accommodated along low-angle faults [*J. Kapp et al*., 2005]. The northern Gulu segment shows a kinematic linkage with the Beng Co fault, a ~122° striking dextral strike-slip fault, made up of two main fault strands ~40 km in length, which cuts obliquely across previously shortened Jurassic-Cretaceous rocks [*Girardeau et al*., 1984; *Armijo et al*., 1986, 1989]. The largest observable offsets along the Beng Co fault are at its northern extremity where there is at least 7.5 km of dextral offset [*Armijo et al*., 1986, 1989]. A recent investigation indicates a fault slip rate of ~1 mm a^{-1} based on optically stimulated luminescence dating and offset reconstruction of faulted paleoshorelines [*Hollingsworth et al*., 2010]. Assuming the 1 mm a^{-1} slip rate represents the long-term geologic rate implies an initiation age for the Beng Co fault at ~7.5 Ma (Hollingsworth et al., personal communication).

[14] The Pum Qu-Xainza and Tangra Yum Co rifts to the west are the least documented of the major rifts in southern Tibet. Both rifts are composed of various segments that cut across central to southern Tibet and through the IYS where the topographic expression becomes subdued, before continuing into the Himalaya. Zircon U-Pb and apatite and zircon (U-Th)/He ages for the northern portion of the Xainza rift flank record the onset of extension at 14 Ma, as well as a later episode of accelerated exhumation between 10 and 6 Ma; rift morphology and thermochronological observations suggest there is less than 10 km of exhumation (Hager, personal communication). In the central section of this rift there is seismic evidence for active low-angle normal faulting [*Monigle et al*., 2012]. In the Tangra Yum Co rift, apatite and zircon (U-Th)/He ages suggest two distinct episodes of extension and footwall cooling at 13 and 6 Ma, with the latter being more dominant and interpreted to reflect the development of the modern rift topography [*Dewane et al*., 2006]. The magnitude of extension accommodated by the Tangra Yum Co rift is unknown. To the north, both rifts show apparent kinematic linkages to different fault splays of the Gyaring Co dextral strike-slip fault, which itself displays at least 12.5 ± 4 km of separation along its northwestern segment [*Taylor et al*., 2003].

[15] Additional timing constraints for the onset of east-west extension outside southern Tibet include the Shuang Hu Graben in central Tibet and multiple Himalayan rifts to the south (Figure 1). The northeast trending Shuang Hu rift is the only extensional structure in central Tibet with published timing constraints, exhibiting a minimum age for the onset of east-west extension at 13.5 Ma [*Blisniuk et al*., 2001]. Within the Himalaya, north trending rifts exhibit timing estimates for the onset of extension similar to those in Tibet, as well as evidence for accelerated rates of extension postdating the timing of rift inception [*Garzione et al*., 2000; *Murphy et al*., 2002; *Thiede et al*., 2006; *Kali et al*., 2010; *Lee et al*., 2011; *Langille et al*., 2012] (Figure 1).

2.1.1. Geology of the North Lunggar Rift

[16] The Lunggar rift is located in the western region of southern Tibet and is the most developed rift in the Lhasa terrane west of Yadong-Gulu, consisting of a northern section (North Lunggar) [*Kapp et al*., 2008] (Figures 1 and 3a) and a southern section (South Lunggar) [*Styron et al*., 2013]. The North Lunggar range is ~70 km long north-south and 15–25 km wide east-west (Figure 4). The northern extent of the North Lunggar range consists of Paleozoic-Mesozoic sedimentary and metasedimentary rocks (Pz-Mz). The central and southern parts of the range are composed of variably deformed Cretaceous-Miocene granites (gr) and orthogneisses and paragneisses (ma).

[17] The North Lunggar range is the footwall of an east dipping low-angle normal fault in the central part of the range (herein referred to as the North Lunggar detachment), which is interpreted to be the master fault of the rift. The North Lunggar detachment juxtaposes variably deformed granitic (gr) and gneissic (ma) units in its footwall with Cretaceous sedimentary and Tertiary volcanic rocks (K) in its hanging wall. From structurally higher to lower levels, the ~meter-thick detachment fault zone consists of clay gouge, chloritic breccia, cataclasite, and rare pseudotachylites. These features overprint ductile structures, consistent with a transition from ductile to brittle deformation of the footwall

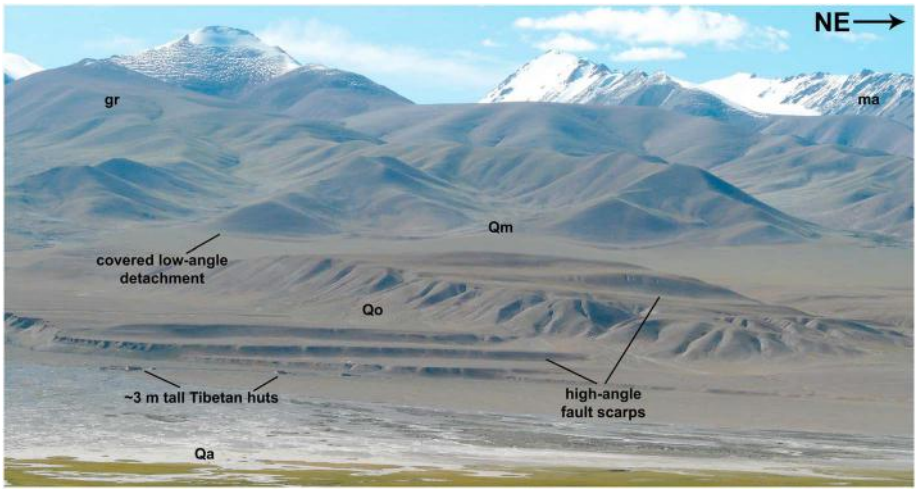

Figure 5. Northwest facing view of the North Lunggar footwall and rift valley showing covered low-angle detachment and basinward stepping of active high-angle normal faulting. Unit labels are the same as those in Figure 3.

during progressive cooling and exhumation [e.g., *Lister and Davis*, 1989]. The shallowest extent of the North Lunggar detachment is interpreted to be inactive at the range front, as it is unconformably overlain by undeformed glacial moraines and cobble-boulder conglomerates [*Kapp et al.*, 2008]. Active surface extension is accommodated in the rift valley 2–5 km east of the range-bounding detachment where antithetic and synthetic normal faults exhibit up to 50 m of throw on individual fault scarps that strike subparallel to the inactive low-angle detachment; these faults have been interpreted to sole into the North Lunggar detachment, which is active at depth [*Kapp et al.*, 2008] (Figure 5). The central portion of the rift footwall exhibits an ~3 × 10 km swath of Neogene growth strata (N-Q) that are stranded in the detachment footwall with stratal dips steepening toward the rift valley, consistent with horizontal-axis rotation associated with a rollover geometry and basinward stepping of active high-angle faults. High-angle normal faults also bound the North Lunggar footwall at the northern and southern tips of the eastern range front, as well as along the western flank of the range (Figure 4). Structural and kinematic measurements were taken on brittle and ductile structures in the footwall and brittle fault planes in the hanging wall. Fault plane orientations, striations, foliations, and lineations were analyzed using lower hemisphere equal area stereonets (plotted with Stereonet 9 v. 6.3.3 by Richard Allmendinger). Some measurements appear

Table 1. Zircon U-Pb Geochronology

Sample	Latitude	Longitude	Age (Ma)	± (Ma)	Rock Type
			This study		
82109PK1	31.66348	83.66363	152.0	1.0	quartzofeldspathic intrusion
82209PK1	31.72810	83.57302	152.3	2.4	granodiorite
82309PK1	31.57888	83.53557	13.3	1.3	biotite granite
82309PK2	31.57873	83.53150	14.1	0.3	leucogranite
82309PK3	31.57865	83.52555	14.4	0.2	mylonitic leucogranite
82309PK4	31.57967	83.51840	14.9	0.7	mylonitic leucogranite
82309PK5	31.57997	83.51008	14.5	0.6	mylonitic leucogranite
82409PK1	31.95570	83.75857	111.0	1.2	rhyolitic tuff
82409PK2	31.95570	83.75857	145.5	1.9	porphyritic rhyolite
82609PK1	31.52405	83.53183	13.8	0.4	mylonitic granite
82609PK4	31.52655	83.51908	13.2	0.6	leucogranite
82609PK5	31.53467	83.52292	13.0	0.4	biotite granite
82609PK6	31.53167	83.52068	13.1	0.6	weakly foliated biotite granite
82709PK2	31.43487	83.56398	123.8	2.8	biotite granite gneiss
82709PK3	31.60135	83.27952	154.4	2.5	granodiorite
82809PK1	31.48203	83.54698	126.7	1.3	green volcanic
82909PK1	31.87800	83.70422	144.2	1.5	quartz sanidine volcanic
82909PK2	31.80408	83.79282	145.9	2.2	quartz-plagioclase volcanic
			Kapp et al. [2008]		
6-7-05-2	31.57872	83.53848	8.9	0.2	mylonitic leucogranite
6-7-05-3	31.57835	83.53970	9.0	0.2	mylonitic leucogranite
6-9-05-2	31.81572	83.65753	152.0	2.0	granite
6-11-05-1B	31.61040	83.53837	15.2	0.4	mylonitic leucogranite
6-15-05-3	31.47942	83.56945	21.7	0.6	biotite granite

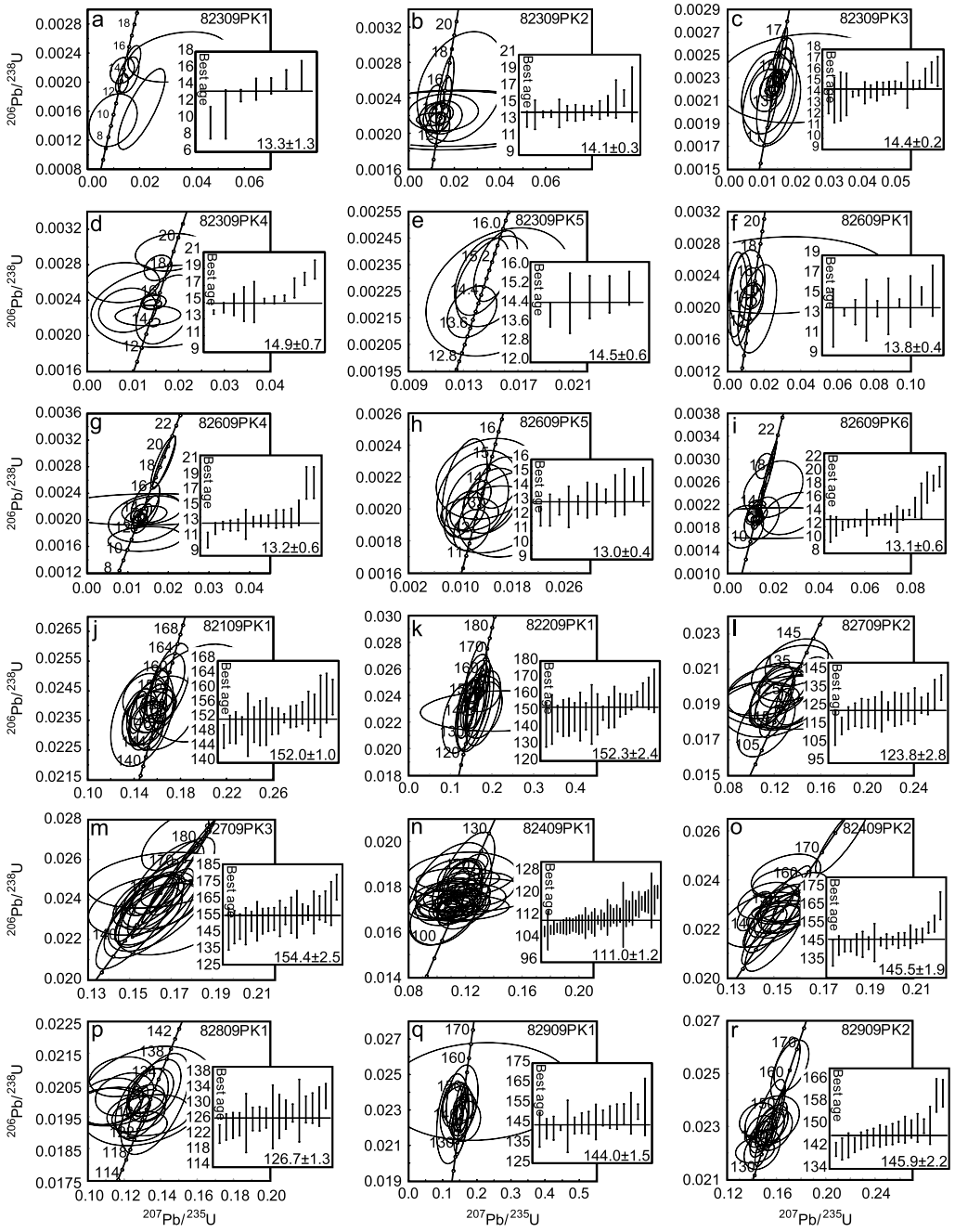

Figure 6. Zircon U-Pb Concordia plots and weighted mean ages for (a–i) footwall plutonic, (j–m) nonfootwall plutonic, and (n–r) volcanic samples from the North Lunggar rift.

oblique to those mapped, due to the scale of the mapping, variability within the shear zone, or potentially representative of a previous tectonic regime (such as the southwest dipping measurements in the south) (Figure 4). The overall fault kinematic data consistently show east-west extension accommodated on both high- and low-angle normal faults, with dominantly top-to-the-east shear sense in the footwall (Figure 4).

[18] The adjacent 5–10 km wide rift valley contains an east-west trending topographic high composed of older lacustrine (Qo) sediments capped by younger fluvial deposits (Qa). This topographic high is a drainage divide with rivers flowing to basins located to the northern and southern terminations of the rift. The transition from deposition to erosion and incision has been interpreted to represent basin inversion due to isostatic uplift of the underlying detachment footwall in response to tectonic unloading [*Kapp et al*., 2008].

[19] Piercing points are generally lacking for quantifying horizontal extension for the North Lunggar rift. As discussed in *Styron et al*. [2013], an absolute maximum value for horizontal extension can be obtained by measuring between undeformed volcanics on opposite sides of the range, perpendicular to strike. This yields a maximum value for horizontal extension of 25–30 km. A more likely estimate is given by measuring between the undeformed hanging-wall strata, which gives an estimate of 15–20 km in the northern and central sections of the range, and ~10 km in the southern section,

north of the accommodation zone between the North and South Lunggar rifts.

[20] To the north, the North Lunggar rift is kinematically linked to the ~150 km long, ~125° striking Lamu Co dextral strike-slip fault [*Taylor et al*., 2003]. The Lamu Co fault appears to be active based on fault scarps and triangular facets visible in satellite imagery indicating Neogene dextral slip [*Taylor et al*., 2003] and satellite geodetic data using InSAR consistently showing modern dextral motion along the fault [*Taylor and Peltzer*, 2006]. The northwestern segment is curvilinear in map view with two right-stepping segments resulting in a prominent pull-apart basin [*Taylor et al*., 2003]. East striking Jurassic volcanic strata associated with a south directed thrust fault is truncated on both sides of the Lamu Co fault indicating 17 ± 5 km of dextral separation [*Cheng and Xu*, 1987; *Taylor et al*., 2003] (Figure 3b). To the southeast, the ~6 km offset thrust belt is unambiguous in satellite imagery; however, its offset may be less than those mapped by *Taylor et al*. [2003] due to smaller, ancillary structures to the northwest of the North Lunggar rift that accommodate eastward motion.

[21] Kinematic linkage between the North Lunggar rift and Lamu Co fault may occur through a diffuse zone of faulting where the Lamu Co fault links to both the east dipping master detachment fault on the west side of the rift, as well as minor west dipping faults to the east. A similar situation has been proposed for a kinematic linkage between the Karakoram dextral strike-slip fault and the Gurla Mandhata detachment [*Murphy et al*., 2002], albeit with an oppositely dipping footwall bounding detachment. In both situations a system of strike-slip faults feed dextral motion into north trending normal faults, resulting in a series of small, structurally controlled basins associated with releasing bends [*Murphy et al*., 2002] and an overall geomorphology characterized by depocenters containing large Quaternary lakes, lake sediments, and shorelines that obscure the underlying structure.

[22] To the south, the rift connects to the South Lunggar rift, which is ~70 km along strike, displays opposite polarity for detachment dip (i.e., the main South Lunggar detachment dips to the west), and has accommodated up to 21 km of extension [*Styron et al*., 2013]. The continuation of the North Lunggar rift to the south is not a direct linkage to the South Lunggar rift but rather an accommodation zone between the two that is broken into multiple faults striking both north-south and east-west. The North Lunggar rift continues to the south, trending southeast before tipping out. South of the North Lunggar tip the Surla Range of the South Lunggar rift is bound at its northernmost point by east-west striking normal faults [*Styron et al*., 2013]. Though not explored in detail, the fault geometry suggests there is likely significant distributed right lateral strike slip deformation within the accommodation zone.

3. Zircon U-Pb Geochronology

[23] Zircon U-Pb geochronology was conducted at the University of Arizona LaserChron Center by laser ablation multicollector inductively coupled plasma mass spectrometry following analytical procedures discussed in *Gehrels et al*. [2008]. A total of 23 zircon U-Pb ages were considered for this study: new analysis was conducted on 18 samples (5 volcanic and 13 plutonic; see Table 1 for sample lithologies) in addition to five ages previously published in *Kapp et al*. [2008] (Table 1 and Figure 6). The mean age of the youngest population of zircons is taken to represent the crystallization age for each of the igneous samples.

[24] Plutonic samples reveal two distinct groups of Jurassic-Cretaceous (152–124 Ma) and Miocene (22–9 Ma) ages. The older groups of ages come from samples located on the periphery of the range and the hanging wall of the range-bounding fault system, whereas the Miocene ages are restricted to granites and gneisses in the central part of the footwall of the North Lunggar detachment (Figures 4 and 7a). All of the Miocene leucogranites include older zircon grains that are interpreted to be inherited. Miocene footwall ages are similar to those that have been determined in the footwalls of other detachment faults associated with east-west extension (e.g., Nyainqentanghla, Gurla Mandhata, etc.).

[25] Volcanic rocks yield ages that range from 145 to 110 Ma. These ages are older than previously documented ages for Tertiary volcanic rocks pervasive throughout southern Tibet [*Ding et al*., 2003; *Taylor and Yin*, 2009]; however, ages show overlap with Jurassic-Cretaceous volcanic and intrusive rocks within the northern Lhasa terrane [*Zhu et al*., 2011]. For complete U-Pb geochronometric analysis results and description of analytical methods, see supporting information A.

4. Apatite and Zircon (U-Th)/He Thermochronometry

[26] Low-temperature thermochronology is a powerful approach to dating the cooling and exhumation of footwall rocks in extensional settings [*Stockli*, 2005]. Thermochronometric analysis is now a common way to quantify the timing and rates of faulting [e.g., *Stockli et al*., 2002b] and is especially useful when multiple thermochronometers are used [e.g., *Fitzgerald et al*., 2009]. Apatite and zircon are two of the most commonly used low-temperature mineral thermochronometers, as apatite is the primary host of phosphorous in the crust and thus virtually ubiquitous, and zircon is common in most rock types [*Harrison and Zeitler*, 2005]. Each mineral thermochronometer represents a different structural level in the Earth's crust at which the radiogenic daughter isotope ceases to be lost via thermally activated volume diffusion from its respective mineral crystal lattice [*Farley*, 2002]. The thermal sensitivity window, defined as the zone between the complete retention (accumulation) and complete expulsion (diffusion) of radiogenic ^{4}He from within the mineral crystal and termed the partial retention zone (PRZ) [*Wolf et al*., 1996, 1998; *Stockli et al*., 2000], varies for each thermochronometer; apatite and zircon have PRZs between 40 and 80°C and 130 and 200°C, respectively [*Stockli et al*., 2000; *Reiners et al*., 2004; *Reiners*, 2005; *Wolfe and Stockli*, 2010].

[27] This study incorporates previous analysis on samples from *Kapp et al*. [2008, Data Repository Table DR2] by introducing new apatite and zircon (U-Th)/He ages in addition to the published apatite (U-Th)/He and zircon U-Pb ages for those rocks. Apatite and zircon (U-Th)/He thermochronometric analysis was conducted on 48 samples (232 individual aliquot ages) collected from four detachment-perpendicular footwall transects, as well as various locations in the footwall and hanging wall, and from cobbles within fluvial terraces in the adjacent rift valley (Figures 4 and 7a). Footwall samples are characterized as variably deformed granites and

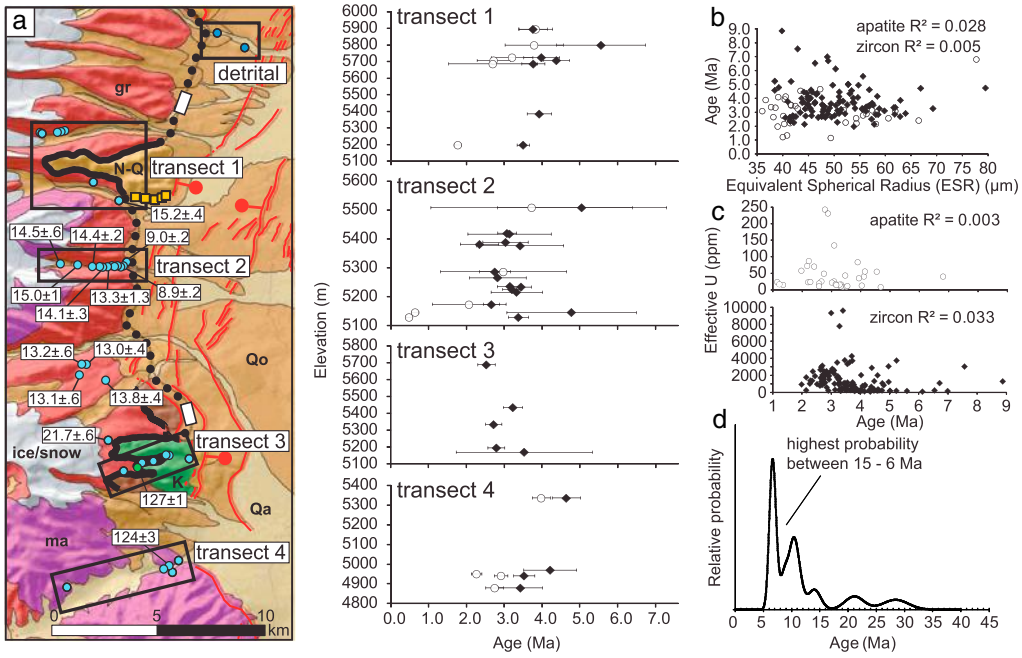

Figure 7. (a) Locations of four detachment-perpendicular footwall transects for the North Lunggar rift and associated age-elevation plots of transects. Map units and symbols are the same as those in Figures 3 and 4. Zircon U-Pb ages are in white boxes on map. For all plots white circles and black diamonds represent apatite and zircon (U-Th)/He ages, respectively. All uncertainties reported are $\pm 1\sigma$ standard deviation of multiple aliquot ages or standard analytical uncertainty ($\pm 2\sigma = 8\%$ zircon, 6% apatite) [*Farley*, 2002]. (b) Age-grain size (equivalent spherical radius, ESR) plot of individual apatite and zircon footwall sample aliquots. Samples show no correlation between age and grain size implying little time spent in the apatite and zircon partial retention zones. (c) Age-effective uranium concentration ([eU]) plot of footwall samples. Results yield no correlation between the two, again consistent with little time spent in the partial retention zone. Despite abnormally high [eU] (>9000 ppm), the lack of negative correlation between age and eU suggests there is no evidence for metamictization due to radiation damage and erroneously young ages due to loss of ^{4}He via fast diffusion pathways [*Reiners et al.*, 2004; *Reiners*, 2005]. (d) Probability density function of detrital zircon thermochronology. Detrital zircon grains from footwall-derived granite boulder clasts collected from fluvial terraces proximal to the footwall yield ages between 28 and 6 Ma with the highest probability between 15 and 6 Ma.

mylonitic gneisses with apatite and zircon cooling ages typically within uncertainty of each other showing late Miocene-Pliocene cooling ages that generally increase with elevation (Figure 7a).

[28] Footwall cooling ages record late Miocene-Pleistocene cooling with apatite and zircon cooling ages between 4.0 ± 0.2 and 0.5 ± 0.1 Ma and 5.6 ± 1.2 and 2.3 ± 0.5 Ma, respectively (Figure 7a) (all uncertainties reported are $\pm 1\sigma$ standard deviation of multiple aliquot ages or standard analytical uncertainty ($\pm 2\sigma = 8\%$ zircon, 6% apatite) [*Farley*, 2002], whichever is greater (Table 2)). Footwall samples are interpreted to have resided below the zircon PRZ until the most recent phase of extension and development of modern topography. The thermochronological data show slight age-elevation correlations (Figure 7a), as expected across extensional rift footwalls [*Stockli*, 2005], but are not significant enough to argue for large amounts of time spent in either the apatite or zircon PRZ, as indicated by the lack of correlation in footwall age versus grain size (equivalent spherical radius, ESR) data (Figure 7b). Similarly, individual aliquot ages plotted against ESR show no correlation ($R^2_{\text{zircon}} = 0.05$ and $R^2_{\text{apatite}} = 0.28$) implying little time spent in the apatite or zircon PRZs due to low kinetic variation in a rapidly cooled system, as smaller grains will preferentially lose ^{4}He if significant time is spent in the PRZ [*Farley et al.*, 1996] (Figure 7b). Zircon parent isotope concentrations have high effective U concentrations ([eU] = [U] + 0.2302[Th] + 0.005[Sm]) that vary from < 300 ppm to > 9000 ppm. Age-[eU] of individual apatite and zircon sample aliquots from the North Lunggar footwall show no correlation; thus, grain-scale characteristics leading to erroneously young ages, such as metamictization [*Reiners*, 2005; *Shuster et al.*, 2006] or enriched rim zoning [*Hourigan et al.*, 2005], are negligible (Figure 7c). Footwall cooling ages vary only slightly along strike, with the youngest ages located in the central to southern portion of the eastern range front.

[29] Within individual sample transects, data show some unexpected results. First, in some cases within the same sample the apatite cooling ages are older than zircon ages (e.g., Figure 7a, transects 1 and 2). This may be due to inclusions within the apatite grains, which can have eU concentrations many times the concentration of pure apatite, resulting in erroneous, "too-old" ages [*Vermeesch et al.*, 2007]. Second, cooling age does not always increase with elevation for individual thermochronometers (e.g., Figure 7a, transect 3). Age-elevation correlation is not a requirement because the age is a function of grain size, radiation damage (for apatite), and

Table 2. Apatite and Zircon (U-Th)/He[a]

Sample	Latitude	Longitude	Elevation (m)	Age (Ma)	± (Ma)	StDev (1σ)	U (ppm)	Th (ppm)	Sm (ppm)	eU (ppm)	Th/U	He (nmol/g)	Mass (µg)	Ft	ESR (µm)
							Apatite								
82309PK1	31.57888	83.53557	5174	2.1	1.0	1.0	28.3	31.5	115.8	36.1	1.6	0.3	1.8	0.6	41.4
82309PK5	31.57997	83.51008	5509	3.7	2.7	2.7	19.6	110.4	123.1	45.6	7.2	0.6	5.2	0.7	57.4
82709PK1	31.43187	83.56398	4951	2.3	0.1	0.1	74.5	11.7	14.1	77.3	0.2	0.7	5.2	0.7	55.3
82709PK3	31.60135	83.27952	4830	46.9	2.8	2.6	31.6	116.0	71.8	58.7	3.7	9.8	2.3	0.6	44.7
KS08310903	31.82720	83.63213	5347	55.9	5.7	5.7	12.2	66.8	108.5	28.1	5.5	5.2	1.5	0.6	39.4
LNG0109	31.43743	83.56670	4880	2.7	0.2	0.2	20.3	9.4	40.5	22.6	0.5	0.2	3.9	0.7	52.4
LNG0209	31.43337	83.55980	4942	2.9	0.2	0.2	179.1	103.1	32.4	203.0	0.6	2.3	4.6	0.7	57.9
LNG0409	31.42470	83.51310	5336	4.0	0.2	0.1	39.2	59.2	121.7	53.4	1.6	0.7	2.6	0.6	38.7
LNG0809	31.45864	83.36063	4854	8.3	2.2	2.2	5.4	19.9	73.5	10.3	3.8	0.3	2.1	0.6	44.2
MT06300601	31.64325	83.50081	5896	3.8	0.4	0.4	25.1	13.0	74.5	28.5	0.8	0.4	4.0	0.6	41.4
MT06300602	31.64263	83.50126	5800	3.8	0.8	0.8	5.7	16.2	22.5	9.5	2.8	0.1	4.1	0.6	43.2
MT06300603	31.64332	83.50899	5726	3.2	0.5	0.5	9.2	6.9	21.1	10.9	0.7	0.1	11.1	0.8	45.8
MT06300604	31.64355	83.51051	5708	2.7	0.4	0.4	26.3	17.4	18.5	30.4	0.6	0.3	7.1	0.7	49.9
MT06300605	31.64389	83.51208	5687	2.7	1.2	1.2	20.6	18.6	37.8	25.0	1.2	0.3	3.8	0.6	42.1
MT07020605	31.57905	83.53473	5287	3.0	1.7	1.7	15.3	57.4	152.6	29.3	3.4	0.4	4.8	0.7	45.1
							Zircon								
z6-11-05-1A	31.61040	83.53837	5199	3.5	0.3	0.3	384.8	165.0	1.0	422.8	8.3	6.5	16.3	0.8	64.7
z6-7-05-2	31.57872	83.53848	5147	4.8	1.7	1.7	663.3	518.5	1.3	782.6	6.0	17.1	6.5	0.8	51.7
z6-7-05-3	31.57835	83.53970	5130	3.4	0.3	0.2	3153.0	399.0	2.4	3244.9	27.8	46.5	7.7	0.8	53.5
z6-9-05-2	31.81572	83.65753	4841	48.8	4.2	4.2	466.7	362.0	1.3	550.1	0.8	107.9	6.2	0.8	50.3
z82109PK1	31.66318	83.66363	4620	63.7	7.3	7.3	246.7	285.3	4.4	312.4	1.9	82.5	5.3	0.8	48.4
z82209PK1	31.72807	83.57302	5404	58.5	4.7	4.1	406.3	277.3	0.9	470.1	0.7	113.5	6.8	0.8	52.9
z82309PK1	31.57888	83.53557	5174	2.7	0.2	0.1	1270.7	545.9	0.6	1396.4	0.4	15.0	4.9	0.7	47.1
z82309PK2	31.57873	83.53150	5217	3.3	0.7	0.7	1489.4	688.0	1.5	1647.8	0.5	23.2	6.0	0.8	49.6
z82309PK4	31.57967	83.51840	5418	3.1	1.1	1.1	833.8	529.1	2.6	955.6	0.6	11.4	4.1	0.7	45.5
z82309PK5	31.57997	83.51008	5509	5.0	2.2	2.2	1102.1	638.6	4.6	1249.1	0.6	25.3	5.2	0.7	47.1
z82409PK1	31.95570	83.75857	4969	92.5	17.7	17.7	174.0	229.7	1.1	226.8	1.3	87.4	4.7	0.7	47.3
z82409PK2	31.95495	83.75870	4956	77.8	7.9	7.9	193.9	185.8	2.1	236.7	1.0	79.0	7.9	0.8	56.1
z82609PK4	31.52655	83.51908	5342	3.4	1.2	1.2	1699.6	1110.3	2.7	1955.2	0.7	28.2	4.9	0.8	47.5
z82609PK5	31.53167	83.52292	5177	5.4	1.2	1.2	2145.4	1759.8	1.9	2550.5	0.8	56.0	4.1	0.7	42.7
z82709PK2	31.43495	83.56242	4971	4.2	0.7	0.7	200.8	72.0	0.3	217.4	0.4	3.7	5.3	0.8	48.0
z82709PK3	31.60135	83.27952	4830	89.3	7.8	7.8	186.5	157.0	0.6	222.7	0.8	88.3	13.0	0.8	65.4
z82809PK1	31.48203	83.54698	5581	17.6	9.8	9.8	73.3	70.8	0.4	89.6	1.0	5.2	9.8	0.8	57.3
z82909PK1	31.87802	83.70422	4840	63.5	11.0	11.0	191.7	192.6	1.3	236.1	1.1	57.1	4.0	0.7	44.7
z82909PK2	31.80408	83.79282	4777	87.1	11.0	11.0	311.0	265.6	1.5	372.2	2.5	132.1	5.9	0.8	49.5
zKS08270901	31.57882	83.52932	5389	3.0	0.6	0.6	2241.6	471.5	0.6	2350.1	17.1	31.4	5.8	0.8	47.9
zKS08270903	31.57922	83.54046	5235	3.4	0.3	0.3	2814.4	596.2	4.2	2951.6	17.2	41.7	5.1	0.8	47.7
zKS08280901	31.48813	83.56200	5172	3.5	1.8	1.8	1125.0	126.2	0.4	1154.0	6.0	11.9	4.8	0.7	45.8
zKS08280902	31.48801	83.56088	5197	2.8	0.2	0.2	1406.5	918.2	1.2	1617.8	7.3	18.2	3.9	0.7	44.4
zKS08280905	31.48449	83.54921	5436	3.2	0.3	0.2	8801.0	509.6	0.3	8918.3	45.8	120.2	5.4	0.8	50.9
zKS08280907	31.48035	83.54049	5689	2.5	0.2	0.2	1371.7	538.2	0.4	1495.6	6.6	14.9	3.6	0.7	44.3
zKS08300901	31.61937	83.52605	5386	3.9	0.3	0.3	867.8	134.9	1.0	898.9	0.2	14.4	6.2	0.8	50.1
zKS08310901	31.81522	83.65599	4896	39.7	3.8	3.8	261.7	181.0	0.6	303.4	0.7	50.6	5.6	0.8	49.8
zKS08310903	31.82720	83.63213	5347	63.3	5.1	2.3	191.1	171.7	0.9	230.6	0.9	62.0	8.8	0.8	57.3
zKS08310904	31.82817	83.63034	5371	3.1	0.3	0.3	988.5	1041.6	1.8	1228.3	1.0	15.9	8.0	0.8	55.3
zLNG0109	31.43743	83.56670	4880	3.4	0.6	0.6	188.0	95.6	0.3	210.0	0.5	3.0	7.4	0.8	53.8

Table 2. (continued)

Sample	Latitude	Longitude	Elevation (m)	Age (Ma)	± (Ma)	StDev (1σ)	U (ppm)	Th (ppm)	Sm (ppm)	eU (ppm)	Th/U	He (nmol/g)	Mass (µg)	Ft	ESR (µm)
zLNG0209	31.43337	83.55980	4942	3.5	0.3	0.2	316.6	117.3	0.3	343.6	0.4	5.0	5.7	0.8	49.3
zLNG0409	31.42470	83.51310	5336	4.6	0.4	0.1	255.8	79.8	0.3	274.2	0.3	5.3	8.5	0.8	55.3
zLNG0809	31.45864	83.36063	4854	35.6	8.8	8.8	228.4	195.3	1.9	273.4	0.9	42.5	5.2	0.8	48.6
zMT06300601	31.64325	83.50081	5896	3.8	0.4	0.4	398.7	105.0	0.8	422.9	0.3	6.4	5.8	0.8	47.9
zMT06300602	31.64263	83.50126	5800	5.6	1.2	1.2	133.1	110.4	0.7	158.5	0.8	3.7	5.7	0.7	47.5
zMT06300603	31.64332	83.50899	5726	4.0	0.5	0.5	386.0	177.8	1.3	427.0	0.5	6.7	11.1	0.8	47.7
zMT06300604	31.64355	83.51051	5708	4.4	0.4	0.3	216.0	143.2	1.1	249.0	0.7	4.6	7.7	0.8	53.9
zMT06300605	31.64389	83.51208	5687	3.8	0.3	0.2	284.7	160.8	1.1	321.8	0.6	4.9	5.7	0.8	48.4
zMT07020601	31.57873	83.52893	5420	3.1	0.2	0.2	1707.7	609.9	4.3	1848.1	0.4	22.9	5.8	0.8	50.0
zMT07020603	31.57872	83.53054	5377	3.4	1.2	1.2	1779.9	672.4	2.5	1934.7	0.6	25.5	10.8	0.8	57.7
zMT07020604	31.57869	83.53264	5382	2.3	0.5	0.5	1379.1	574.6	3.6	1511.4	0.4	15.0	4.9	0.8	48.2
zMT07020605	31.57905	83.53473	5287	2.7	0.4	0.4	1706.6	841.4	4.5	1900.4	0.4	22.4	7.3	0.8	54.1
zMT07020606	31.57916	83.53745	5267	2.8	0.8	0.8	2168.7	645.7	9.9	2317.4	0.4	30.9	9.2	0.8	56.7
zMT07020607	31.57914	83.54036	5237	3.1	0.3	0.3	1374.2	300.0	3.0	1443.3	0.4	18.5	7.4	0.8	52.6
zMT07020608	31.58077	83.54194	5226	3.2	0.3	0.1	1630.2	555.6	30.0	1758.2	0.4	23.8	8.2	0.8	55.5
zMT06170601	31.68391	83.59858	detrital												
zMT06170602	31.69093	83.58551	detrital												

[a]Ft = alpha ejection correction following *Farley et al.* [1996]; ESR = equivalent spherical radius; eU = effective U.

zonation. If all minerals were the same size and chemical composition, then lower samples should always be younger, although differences in diffusion kinetics will have lesser influence on the age spread when the samples are rapidly cooled, as in the case of the North Lunggar footwall. Younger, higher-elevation samples may be the result of enriched rims or cracked grains for zircon (possibly for sample zKS08280907 in transect 3), abnormally high eU, and thus more retentive grains for apatite (possibly for sample LNG0209 in transect 4), or given the scale and lack of detailed mapping, obscured or unidentified geologic structures between samples within transects. Third, apatite samples for transect 2 are very young (0.5–0.6 Ma). When compared to the other apatite ages, there is an expected age-elevation correlation; however, the small elevation distance between the samples requires extremely high cooling rates. These samples were among the smallest grains processed (mean ESR $\leq$ 40 µm), which could result in abnormally young ages [*Farley et al*., 1996], or these ages may have been reset by hot fluid circulation, as they are also the closest samples to the detachment. These types of inconsistencies in the data can be explained individually; however, they inevitably present problems when interpreting and modeling the data (see section 5).

[30] Samples with cooling ages older than middle Miocene are volcanic rocks, granitic intrusions, and sedimentary rocks which yield zircon ages that document cooling from 92.5–63.7 Ma (Figure 4). These rocks are interpreted to have resided below the closure temperatures (structurally above the PRZs) for respective thermochronometers before the onset of extension. Paleozoic-Mesozoic sedimentary to metasedimentary units from the northern portion of the North Lunggar footwall yield zircon He ages of 63.3–39.7 Ma and apatite He ages of 55.9–5.1 Ma. Two samples from granitic bodies on the southwest side of the range (LNG0809 and 82709PK3 in Figure 4) yield zircon He ages between 89.3 and 35.6 Ma and apatite He ages between 46.9 and 8.3 Ma, respectively. These results support recent work showing that plateau-like conditions may have been reached in central Tibet by 45 Ma and that erosion rates were minimal throughout the Cenozoic [*Rohrmann et al*., 2012]. The spatial distribution of syn-extensional and pre-extensional cooling ages is consistent with extension and exhumation caused by rollback and abandonment of the footwall and basinward stepping of active faulting. Features such as these located in the northeastern range front where there are much older ages within the North Lunggar range are interpreted to be fault-bounded hanging-wall slivers [e.g., *Wernicke and Axen*, 1988]. This is evident in the northern section of the footwall (Figure 4) where the transect is dominated by sedimentary strata exhibiting much older cooling ages. The majority of this transect yields older ages interpreted to be unreset hanging-wall material that was transferred to the footwall during rift evolution. Because these cooling ages likely represent a cooling history that precedes the onset of regional extension, thermal modeling of this northern transect was not conducted.

[31] Detrital zircon grains from footwall-derived granite cobbles collected from fluvial terraces adjacent to the North Lunggar range front yield (U-Th)/He cooling ages between 28 and 6 Ma with a distribution showing the highest probability between 15 and 6 Ma (Figure 7d). The source elevation of

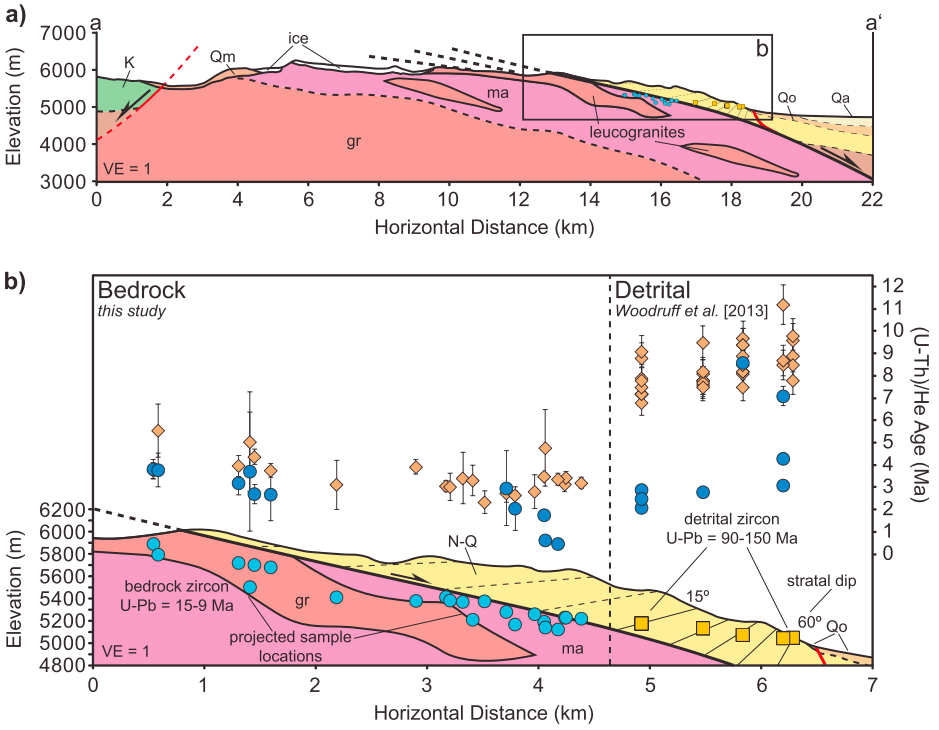

Figure 8. (a) Cross section a-a′ through the North Lunggar footwall and growth strata. (b) Age-elevation-relationship (AER) plot of bedrock (light blue circles; this study) and detrital (orange squares) [*Woodruff et al*., 2013] (U-Th)/He cooling ages (dark blue circles = apatite; orange diamonds = zircon).

these cobbles and the age of the fluvial terraces from which they were collected are unknown; the only possible catchment to source them resides beneath the glaciers from the North Lunggar footwall itself. Detrital ages presented here are consistent with the more extensive detrital zircon (U-Th)/He thermochronologic data set from the North Lunggar rift by *Woodruff et al*. [2013], who interpret an inverted age-elevation distribution from the growth strata in the central North Lunggar footwall as indicating initiation of extension earlier than 10 Ma (Figure 8). The age distributions from bedrock samples and ages from detrital data sets have little to no overlap. The majority of detrital ages presented here (supporting information Table B1) and in *Woodruff et al*. [2013, Table DR2] are interpreted to represent the paleo-PRZ from before and during early stages of extension found updip of the North Lunggar footwall, which is currently inaccessible due to active glaciation (Figure 9). Though our detrital data set is not extensive, it is further evidence that extension was underway by 10 Ma. For ages of individual aliquots for all apatite and zircon (U-Th)/He ages and description of analytical methods see supporting information B.

5. Thermal Modeling

[32] The field of thermochronology has evolved considerably in the past decade, and advances in thermal modeling techniques have provided ways to quantify thermal histories with greater confidence [*Ehlers*, 2005]. In addition to yielding more meaningful and robust results, thermal modeling provides statistical significance and a means to quantify cooling rates—a necessity to reliably constrain the thermal history from thermochronometric data sets. Tectonic interpretations drawn from age-elevation plots alone assume elevation is a viable proxy for depth, though this is not usually the case in actively deforming regions [*Clark et al*., 2010]. Here we present results using two different techniques: the first to determine the t-T cooling history and plausible values for geothermal gradient for individual sample transects and the second to determine a viable exhumation rate and magnitude resulting in transient geothermal gradient estimates for comparison to the first model.

5.1. Helium Modeling Package Methodology and Model Setup

[33] Thermochronometric data from the North Lunggar footwall were first modeled using the MATLAB-based Helium

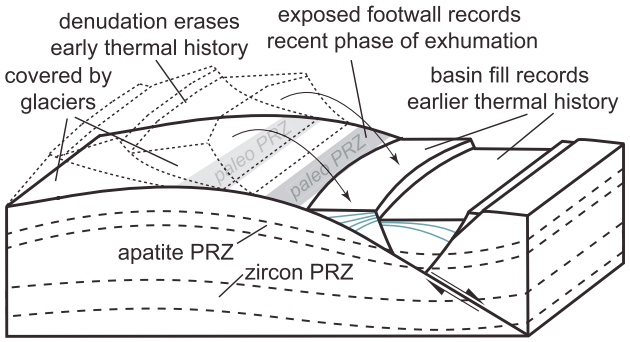

Figure 9. Block model after *Kapp et al*. [2008] showing how rotation and denudation of the North Lunggar footwall erases evidence for an earlier rift inception that is preserved in the adjacent rift valley.

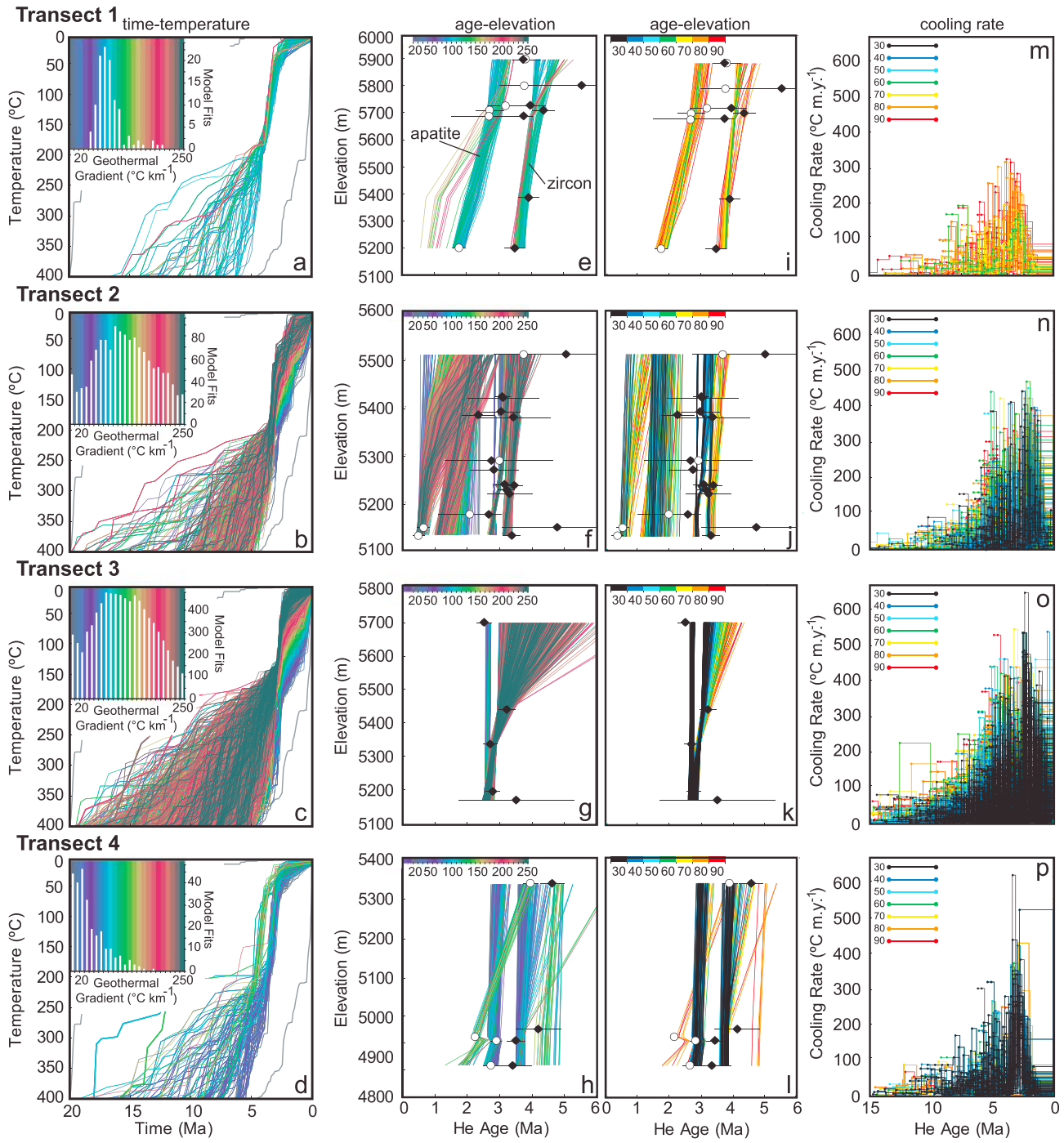

Figure 10. HeMP thermal modeling results for footwall transects 1–4. (a–d) Results for acceptable t-T path fits for each geothermal gradient (20–250°C km^{-1}) based on the goodness-of-fit criterion [*Ketcham et al.*, 2000]. (e–h) Age-elevation model fits for all acceptable HeMP model fits; white circles and black diamonds represent apatite and zircon (U-Th)/He ages, respectively. (i–l) Acceptable age-elevation model fits for geothermal gradients 30–90°C km^{-1}. (m–p) Cooling rates for acceptable model fits for geothermal gradients 30–90°C km^{-1}.

Modeling Package (HeMP) [*Hager and Stockli*, 2009]. HeMP uses randomly generated t-T paths to find matching thermal histories for multiple thermochronometers from single samples or sample transect arrays based on the algorithms described in *Ketcham* [2005]. Model fits are based on a goodness-of-fit criterion (Kolmogorov-Smirnov test) utilized by HeFTy [*Ketcham et al.*, 2000]; good model fits correspond to values ≥0.50; acceptable fits correspond to values ≥0.05. Essentially, good model fits imply the t-T path and associated geothermal gradient is *supported by the data*, while acceptable fits are *not ruled out by the data* [*Ketcham et al.*, 2000; *Ketcham*, 2005]. HeMP modeling

software has been successfully used to derive the t-T history of rift footwalls using apatite and zircon (U-Th)/He data [e.g., *Lee et al*., 2011].

[34] Required model inputs were mean values from aliquot analyses for age and uncertainty, parent isotopic concentration, grain size, and sample elevation, as well as a range of user-defined geothermal gradients. The HeMP model incorporates the He trapping model (radiation damage accumulation and annealing model) [*Flowers et al*., 2009] for apatite data to account for natural influences in radiation damage and associated increased retentivity in apatite [*Shuster et al*., 2006]. Model precision was set to 3.5°C and 0.1 Ma increments, with 50,000 random t-T paths generated through 15 random points between model constraints. The number of outliers (each outlier is the entire sample, i.e., both apatite and zircon cooling ages) allowed varies depending on transect data characteristics, cooling age uncertainty, and age-elevation correlation. To constrain the highest probability for geothermal gradient based on the number of model fits, a range in geothermal gradients from 20 to 250°C km^{-1} were modeled with 10°C increments for each transect. Start time was set between 20 and 5 Ma. Models were initially tested beginning at the U-Pb closure temperature of 720°C [*H. Zhang et al*., 2004]; however, results were virtually unconstrained between that temperature and 400°C due to the lack of mid-temperature thermochronometric constraints (e.g., ^{40}Ar/^{39}Ar), and less precisely constrained t-T paths through the apatite and zircon PRZs. Thus, the model start temperature was set to 400°C, representing the approximate depth to the brittle-ductile transition at 13–16 km assuming a pre-extensional geothermal gradient of 25–30°C km^{-1}. Mineral assemblages of these rocks show they were never subjected to amphibolite facies pressure-temperature conditions deeper than the upper middle crust, so a starting temperature of 400°C is considered reasonable. End temperature was set to 5 ± 5°C for all model runs, representing Earth's mean annual surface temperature. No additional restrictions in t-T space were placed on the models.

[35] Footwalls of low-angle normal faults often undergo rotation and flexure, requiring that low-temperature thermochronologic data be compared to a paleo-horizontal datum [e.g., *Reiners et al*., 2000; *Stockli et al*., 2003]. Such rotations will particularly affect estimations of exhumation rates and to a lesser degree the onset of rapid exhumation, which are critical to the interpretations made here. To account for this, we tested HeMP models with different elevation corrections to simulate 10–30° of footwall rotation. Results yield virtually no change in the resulting t-T paths and geothermal gradients due to the tightly constrained window of apatite and zircon cooling ages, so the original field sample elevations were used (Table 2).

5.2. HeMP Model Results

[36] HeMP model t-T paths (Figures 10a–10d) and associated age-elevation results (Figures 10e–10h) are plotted for all modeled geothermal gradient values that yielded acceptable fits for each transect. Inconsistencies within individual transects in this data set complicate the modeling by presenting complexities beyond the capability of the thermal model and requiring some data to be disregarded. For the HeMP model, this is done in the form of assigning the number of outliers allowed for individual transects. A sample may be an outlier for one t-T path, or a fit for another, which is why the frequency of model fits is important for both good and acceptable results, though less so for the latter. It is possible to model samples with apatite ages older than zircon because in this data set these same-sample ages are always within uncertainty of each other. Age-elevation correlation is also not a requirement (see section 4). In order for the model to yield good model fits based on the goodness-of-fit criterion [*Ketcham et al*., 2000], an unreasonable amount of model outliers were required (> 50% samples for each transect), likely due to the closeness/overlapping apatite and zircon cooling ages. Results from model runs with such a large number of outliers varied inconsistently, yielding very different and inconclusive results. Models set up with fewer outliers and yielding only acceptable model fits provided consistent results for both geothermal gradient and cooling rate and fit the age-elevation data more precisely. Thus, achieving good model fits was not considered a necessity for this data set, and models yielding acceptable fits with the minimum number of outliers were used for further interpretation.

[37] Transect 1 had two outliers (out of seven samples), transect 2 had four outliers (out of 15 samples), transect 3 had one outlier (out of five samples), and transect 4 had two outliers (out of five samples). The HeMP software uses a fixed geothermal gradient through time; these values are interpreted to represent a dynamic (i.e., transient) geothermal gradient in and around the PRZ for a thermochronometer when a sample passed through it, as this is the best constrained part of the HeMP model given the input data. Results for geothermal gradient are highly nonunique, as very high values for geothermal gradient yield very low values for exhumation rate and cumulative exhumation, and vice versa. Results for t-T paths and associated cooling rates are consistent regardless of the geothermal gradient tested (20–250°C km^{-1}) (Figures 10a–10d). Results yielding t-T paths with higher cooling rates (> 500°C Ma^{-1}) typically corresponded to a lower frequency of model fits for geothermal gradient.

[38] As discussed above, HeMP model results only yielded acceptable fits, meaning model fits are not ruled out by the data, and also they are not necessarily supported by the data [*Ketcham et al*., 2000; *Ketcham*, 2005]. High values for transient geothermal gradient (e.g., > 100°C km^{-1}) may be achieved in detachment systems [e.g., *Gottardi et al*., 2011], but these values are extremely short lived and not representative of the mean geothermal gradient. Plausible values for geothermal gradient were bracketed using a 1-D thermal model for transient geothermal gradient (see section 5.3 below). Cooling path results were reduced to model fits associated with reasonable geothermal gradient values from the 1-D model between 30 and 90°C km^{-1}. These model fits show more consistency with the age-elevation data (Figures 10i–10l) and similar cooling rates for all model fits (Figures 10m–10p).

[39] HeMP model results for temperatures > 200°C are relatively unconstrained. For all four transects the timing of cooling through temperatures > 350°C is essentially constrained by the model input parameters. The timing of cooling through 300°C varies from 17.1–12.1 Ma on the upper end to 4.6–2.9 Ma on the lower end. Model results are better constrained for passage through the zircon and apatite PRZs. All transect model results show the most rapid

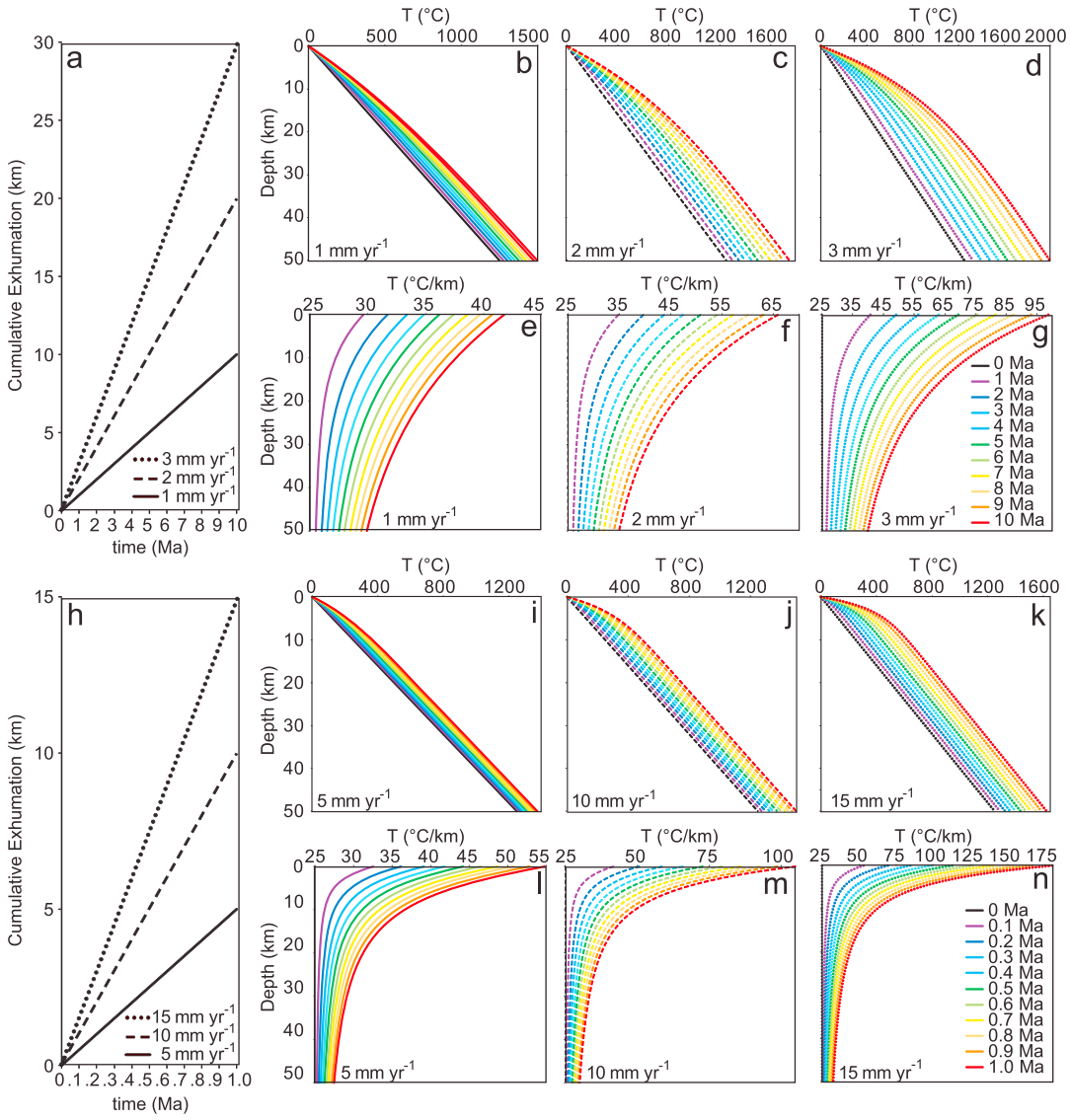

Figure 11. Calculations for transient subsurface temperature using the 1-D transient advection-diffusion equation [*Ehlers*, 2005] calculated every 100 m from 0 to 50 km. (a) 10, 20, and 30 km cumulative exhumation resulting from 1, 2, and 3 mm a^{-1} exhumation for 10 Ma, and associated (b–d) transient subsurface temperatures and (e–g) geothermal gradients that vary with depth. (h) 5, 10, and 15 km cumulative exhumation resulting from higher exhumation rates of 5, 10, and 15 mm a^{-1} exhumation for 1 Ma, and associated (i–k) transient subsurface temperatures and (l–n) geothermal gradients that vary with depth.

cooling rates (as high as 400–500°C Ma^{-1}) between 5 and 2 Ma (Figures 10m–10p). Model results show this was most recent for transects 2 and 3 in the center of the North Lunggar footwall and slightly earlier for transects 1 and 4 to the north and south. Transect 1 passed through the maximum zircon thermal window (200°C) and the minimum apatite thermal window (40°C) at 4.6 ± 0.6 and 2.6 ± 0.4 Ma; transect 2 at 3.6 ± 0.8 and 1.2 ± 1.1; transect 3 at 4.9 ± 2.4 and 1.4 ± 1.3; and transect 4 at 6.7 ± 3.2 and 2.7 ± 0.7.

5.3. 1-D Transient Geothermal Gradient Calculation

[40] To place constraints on transient geothermal gradient, exhumation rate, and slip magnitude for the North Lunggar rift, we used the 1-D transient advection-diffusion equation [*Carslaw and Jaeger*, 1959]:

$$\alpha \frac{\partial^2 T}{\partial z^2} = \frac{\partial T}{\partial t} + v \frac{\partial T}{\partial z} \tag{1}$$

[41] In this equation α is thermal diffusivity, T is temperature, z is depth, and v is velocity of the medium relative to the Earth's surface. Equation terms from left to right represent conductive heat transfer, transient heat transfer, and advective heat transfer [*Ehlers*, 2005]. Assuming a constant surface temperature (T_o) at $t = 0$, $z = 0$ and an equilibrium

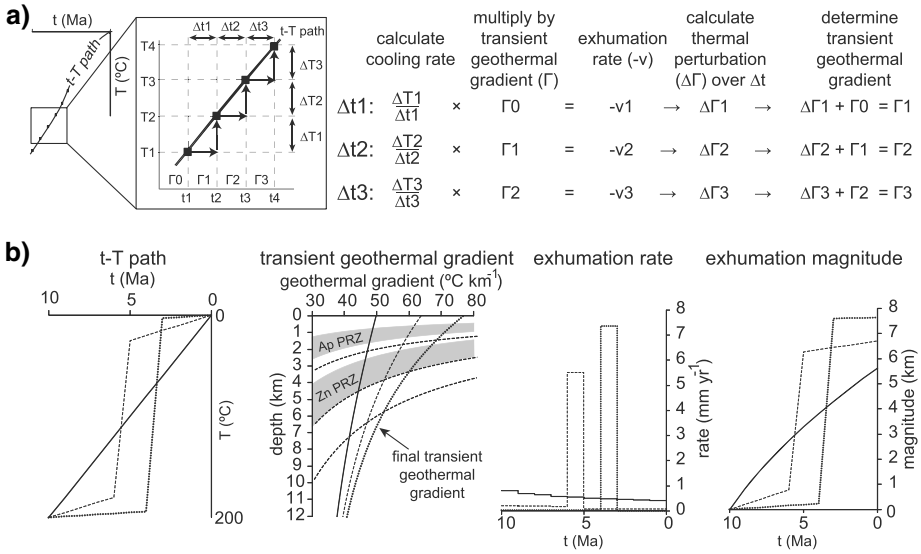

Figure 12. (a) Methodology for deriving transient geothermal gradient from cooling rate by determining the thermal perturbation for a given change in time (see text for details). (b) Example results using three different t-T paths for transient geothermal gradient, and exhumation rate and magnitude.

initial thermal gradient (Γb), equation 1 can be solved for the transient temperature of the subsurface at a specific depth following a period of erosion ($-v$) or sedimentation ($+v$) [*Powell et al*., 1988; *Ehlers*, 2005]:

$$T(z,t) = To + \Gamma b(z - vt) + \frac{1}{2}\Gamma b\left[(z+vt)\exp\left(\frac{vz}{\alpha}\right)\mathrm{erfc}\left(\frac{z+vt}{2(\alpha t)^{\frac{1}{2}}}\right) - (z-vt)\mathrm{erfc}\left(\frac{z-vt}{2(\alpha t)^{\frac{1}{2}}}\right)\right] \quad (2)$$

[42] In equation 2 erfc is the complementary error function [*Abramowitz and Stegun*, 1970]; all other variables are the same as in equation 1. Equations 1 and 2 assume a constant value for thermal diffusivity, despite there being evidence for a decrease in thermal diffusivity with depth from 1.5 to 2.5 $mm^2\,s^{-1}$ at ambient conditions to 0.5 $mm^2\,s^{-1}$ at midcrustal depths [*Whittington et al*., 2009]. Transient geothermal gradients at 10 km depth with a 1 $mm\,a^{-1}$ exhumation rate for 10 Ma decrease by 20.4% (8.7°C km^{-1}) with an increase in thermal diffusivity from 0.5 to 2.5 $mm^2\,s^{-1}$, 1.0% (0.30°C km^{-1}) decrease at 50 km depth. We use 1.3636 $mm^2\,s^{-1}$, the default value used by the Thermochronometer Exhumation Record Recovery Analysis (TERRA) modeling program [*Ehlers et al*., 2005] and a reasonable estimate for crustal rocks [*Whittington et al*., 2009]. Results may underestimate the value for transient geothermal gradient (or overestimate the value for exhumation rate and cumulative exhumation) as this equation solves for the transient geothermal gradient for a homogeneous medium with no radiogenic heat production [*Ehlers et al*., 2005]; however, near-surface effects of heat production are small relative to the effects of advection for moderate (10–12 km) amounts of exhumation [*Mancktelow and Grasemann*, 1997]. To ensure accuracy for solutions to equation 2, we tested a variety of scenarios for comparison to calculations using the Thermal Calculation 1-D Transient module in the TERRA thermal modeling program [*Ehlers et al*., 2005] (see supporting information C for example calculation).

[43] Relative motion between the Earth's surface and uplifting crustal block is assumed to be due to fault activity. There is little to no sedimentation in the rift footwall, so only thermal perturbations in subsurface temperature due to erosion/exhumation were modeled ($-v$). Tectonic exhumation likely far outpaced erosion of the North Lunggar footwall, as erosion rates in Tibet, at least away from the main north trending rifts, were very low (< 0.05 mm a^{-1}) since 45 Ma [*Rohrmann et al*., 2012]. Glacial incision may have affected the shallower apatite cooling ages; however, it was likely not the primary driver of exhumation, as structurally deeper zircon ages show little variability along strike in the North Lunggar rift footwall.

[44] Transient subsurface temperatures were calculated at every 100 m depth from 0–50 km at 1.0 Ma time intervals at 1, 2, and 3 mm a^{-1} for 10 Ma, as well as by 0.1 Ma time intervals at 5, 10, and 15 mm a^{-1} for 1.0 Ma (Figure 11). Transient subsurface temperatures are much more sensitive to thermal perturbation at shallower depths. For example, with an exhumation rate of 1 mm a^{-1} for 10 Ma (10 km cumulative exhumation) at 10 km depth the geothermal gradients increases by a factor of 1.5 but only by a factor of 1.2 at 50 km (Figure 10e). Also, higher exhumation rates yield greater isothermal compression and increased transient geothermal gradients for much shorter durations of time. For the same scenario described above, 10 km of cumulative exhumation could result from a constant exhumation rate of 10 mm a^{-1} over 1 Ma but resulting in a much higher geothermal gradient of 49.2°C km^{-1} at 10 km depth—a factor of 2.0 increase for the same amount of cumulative exhumation (Figure 10m).

[45] Exhumation rate can be established if the cooling rate and geothermal gradient are known. Depending on the rate ($-v$) and duration of exhumation/erosion (Δt), the result is an increase in transient geothermal gradient (thermal

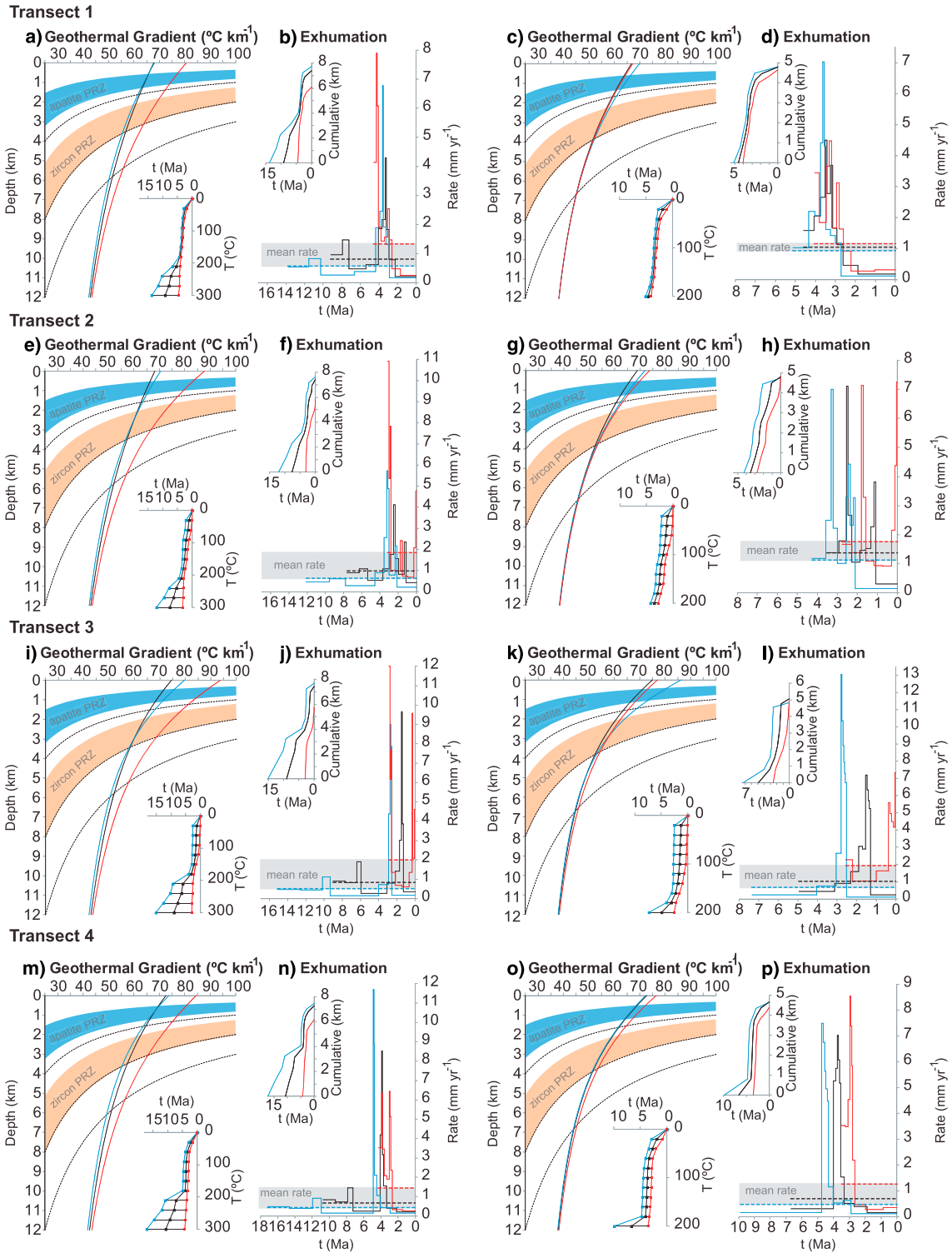

Figure 13. Thermal modeling results for transient geothermal gradient, and exhumation rate and magnitude based on time-temperature (t-T) paths starting at 300°C for (a, b) transect 1, (e, f) transect 2, (i, j) transect 3, and (m, n) transect 4, and t-T paths starting at 200°C for (c, d) transect 1, (g, h) transect 2, (k, l) transect 3, and (o, p) transect 4 using methodology described in Figure 12 (see text for details). Black lines represent results based on mean t-T path from HeMP modeling for each transect; blue = maximum t-T path; red = minimum. Gray boxes bracket the mean rate for each model.

Table 3. Thermal Modeling Results

	Models With Approximated t-T Path Starting at 300°C				Models With Approximated t-T Path Starting at 200°C			
	Timing for Onset of Cooling (Ma)	Transient Geothermal Gradient (°C/km)	Mean Exhumation Rate (mm/yr)	Cumulative Exhumation (km)	Timing for Onset of Cooling (Ma)	Transient Geothermal Gradient (°C/km)	Mean Exhumation Rate (mm/yr)	Cumulative Exhumation (km)
				Mean age t-T Path (black lines in Figure 13)				
Transect 1	9.2	55.5–64.2	0.8	7.4	4.6	51.2–62.0	1.0	4.8
Transect 2	7.6	56.1–64.8	1.0	7.4	3.5	51.2–63.5	1.4	4.8
Transect 3	9.0	56.5–68.1	0.8	7.4	4.9	51.7–67.2	1.0	5.1
Transect 4	10.7	55.8–67.2	0.7	7.3	6.7	51.1–65.6	0.7	4.7
				Maximum age t-T Path (blue lines in Figure 13)				
Transect 1	13.8	54.4–63.9	0.6	7.7	5.1	51.6–64.1	0.9	4.8
Transect 2	12.1	55.3–65.8	0.6	7.6	4.3	52.2–65.6	1.1	4.8
Transect 3	15.1	55.7–71.5	0.5	7.7	7.3	52.1–73.7	0.7	4.8
Transect 4	17.1	54.2–67.0	0.4	7.5	9.9	50.9–65.3	0.5	4.7
				Minimum age t-T Path (red lines in Figure 13)				
Transect 1	4.6	60.4–74.4	1.3	6.1	4.0	51.5–62.5	1.2	4.7
Transect 2	3.1	61.9–79.4	1.9	5.8	2.8	52.5–66.7	1.7	4.8
Transect 3	2.9	62.7–83.3	2.0	5.7	2.5	53.1–69.0	1.9	4.9
Transect 4	4.3	61.2–77.3	1.4	6.1	3.5	52.6–68.5	1.3	4.4

perturbation, $\Delta\Gamma$) for a specified depth (Figure 12a). Repeating this process for multiple $\Delta T\ \Delta t^{-1}$ and summing the $\Delta\Gamma$ gives an estimate for transient geothermal gradient derived from a t-T path and an estimate for exhumation rate and magnitude (Figure 12b).

[46] To apply this technique to cooling paths derived from the HeMP model, cooling rate was estimated every 30°C starting at 300°C and every 20°C starting at 200°C for maximum, minimum, and mean t-T paths (Figure 13). Results calculated at a constant 1 km depth bracket the transient geothermal gradient between 50 and 90°C km^{-1} and cumulative exhumation between 4.4 and 7.7 km (Table 3). Transient geothermal gradient is less sensitive at depth, and so modeling at greater depths yields lower values for transient geothermal gradient and higher values for exhumation rate and cumulative exhumation. For maximum and minimum t-T path approximations (blue and red lines in Figure 13) mean exhumation rates vary between 0.4 and 2.0 mm a^{-1}, with short-lived maximum rates > 10 mm a^{-1} and a minimum 4.4–7.7 km cumulative exhumation (Table 3). Mean t-T path approximations (black lines in Figure 13) yield mean exhumation rates of 0.7–1.4 mm a^{-1} with short-lived maximum rates of 4–10 mm a^{-1} and a minimum 4.7–7.4 km cumulative exhumation (Table 3).

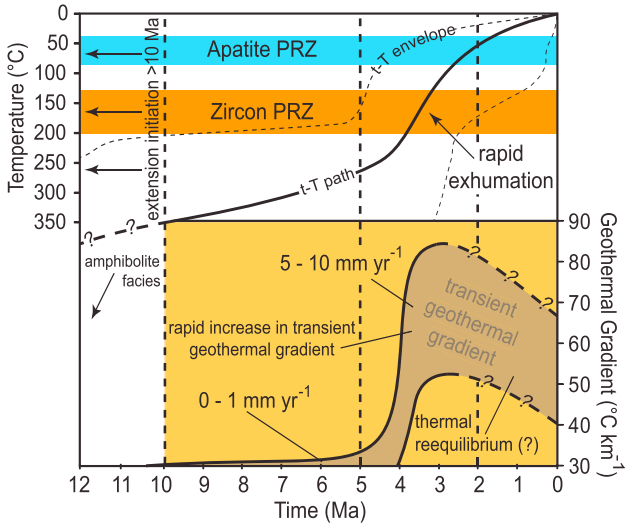

Figure 14. Time-temperature path, onset of extension and rapid cooling for the North Lunggar rift, and associated increase in transient geothermal gradient for the North Lunggar rift during footwall exhumation.

[47] It is widely accepted that extending regions experience compression and decompression of isotherms during stages of acceleration and deceleration of exhumation, respectively [e.g., *Ketcham*, 1996; *Ehlers et al.*, 2001; *Ehlers and Farley*, 2003]. Modeling results for transient geothermal gradient act as a proxy for the thermal structure of the North Lunggar rift and suggest that the apatite and zircon PRZs may be slightly more compressed in the central portion of the North Lunggar footwall than in the south during rapid Pliocene exhumation. There may be slight along-strike differences in thermal structure; however, given the lack of resolution between transects, and the 1-D model used to calculate transient geothermal gradient, there may be more variation than presented here. Assuming a pre-extensional geothermal gradient of 25–30°C km^{-1}, isothermal compression in the North Lunggar footwall is on the order of 1.7–3.6 during rapid exhumation, followed by isothermal decompression and thermal re-equilibration, although the latter remains unconstrained (Figure 14).

6. Discussion

6.1. Structural Style, Initiation, Acceleration, and Magnitude of Extension of the North Lunggar Rift

[48] Geologic and thermochronologic observations show that the central part of the North Lunggar footwall underwent more exhumation and at higher rates than the southern and northern rift tips. This supports preliminary [*Kapp et al.*, 2008] and recent [*Woodruff et al.*, 2013] investigations which concluded that the central part of the rift underwent

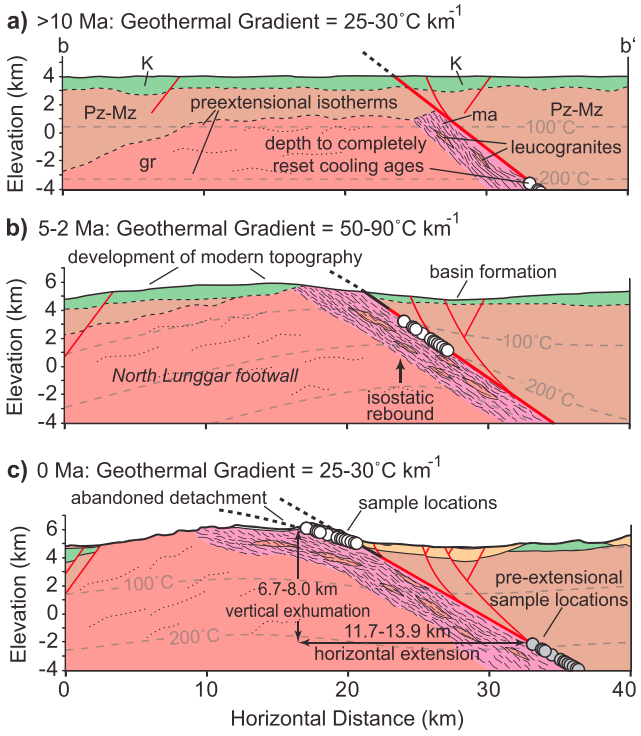

Figure 15. Range perpendicular schematic cross section showing convex-up footwall isotherms and convex-down hanging-wall isotherms during maximum extension and unroofing of the North Lunggar footwall. Assuming a pre-extensional 25–30°C km^{-1} geothermal gradient and a 30° fault dip, the North Lunggar rift has undergone a minimum of 6.7–8.0 km of vertical exhumation and 11.6–13.9 km horizontal extension. Isotherms become compressed by a factor of 1.7–3.6 during periods of rapid exhumation.

isostatic rebound due to rapid centralized extension in the rift, as expressed by the transition from deposition to erosion and incision in the rift valley. There is also evidence for horizontal-axis footwall rotation based on growth strata in the central footwall that steepens toward the hanging wall [*Woodruff et al.*, 2013] (Figure 8). Development of the North Lunggar footwall is best explained by a footwall rebound model [*J. Kapp et al.*, 2005; *Kapp et al.*, 2008], in which rifting begins as a simple half-graben system bound by a high-angle listric fault, followed by isostatic rebound and back-rotation and deactivation of high-angle faults as they are rotated into a low-angle geometry, with younger high-angle faults initiating in the direction of hanging-wall transport [e.g., *Spencer*, 1984; *Wernicke and Axen*, 1988; *Lister and Davis*, 1989] (Figure 9). Similar to many of the rifts that were the basis of the development of the footwall rebound model, the North Lunggar rift is characterized as an extensional metamorphic core complex. Geodynamic [*Buck*, 1988, 1991; *Regenauer-Lieb et al.*, 2006; *Tirel et al.*, 2008] and geologic [*Coney and Harms*, 1984] models predict extensional metamorphic core complexes and associated low-angle normal faults to preferably develop in areas of high elevation and thickened crust. Though these extensional systems develop in a variety of tectonic settings [e.g., *Tucholke et al.*, 1998; *Murphy et al.*, 2002; *Monastero et al.*, 2005], the majority of documented examples are presently inactive and found in areas of low modern elevations and thin crust [*Axen and Bartley*, 1997]. The North Lunggar rift may demonstrate a causal link between active metamorphic core complex development and areas of high elevation, thickened crust acting as a modern analogue to areas that have previously undergone large-magnitude extension.

[49] The North Lunggar rift initiated in middle to late Miocene time based on detrital zircon (U-Th)/He ages between 15 and 6 Ma (Figure 7d). This is consistent with *Woodruff et al.* [2013], who interpret detrital apatite and zircon (U-Th)/He and detrital zircon U-Pb ages from Neogene growth strata in the central section of the North Lunggar footwall and from various locations within the rift valley to show rifting was underway by 10 Ma with a mean rate of 1 mm a^{-1}. Acceleration of the North Lunggar rift took place at 5–2 Ma with the highest cooling and exhumation rates in the center of the range, up to >400°C Ma^{-1} and 4–10 mm a^{-1}. Rapid exhumation resulted in isothermal compression and an elevated transient geothermal gradient of 50–90°C km^{-1}. In order to elevate the geothermal gradient to this level, exhumation rates of >5 mm a^{-1} are required for a relatively short duration of time (0.1–1.0 Ma) (Figure 11), meaning the majority of exhumation took place during Pliocene time.

[50] Assuming a pre-extensional 25–30°C km^{-1} geothermal gradient and a 30° fault dip, the North Lunggar rift has undergone a minimum of 6.7–8.0 km of vertical exhumation and 11.6–13.9 km of horizontal extension (Figure 15). This is similar to the minimum exhumation magnitude calculated in section 5.3 (4.7–7.4 km), which translates to 8.1–12.8 km of horizontal extension using an assumed 30° low-angle fault. If the majority of exhumation and extension occurred since the beginning of the Pliocene (~5.3 Ma), the former estimate yields 2.2–2.6 mm a^{-1}. This is consistent with the minimum mean exhumation rates calculated for the latter (0.7–1.4 mm a^{-1}), which translates to horizontal extension rates of 1.2–2.4 mm a^{-1}.

6.2. Constriction in West Central Tibet

[51] The finite horizontal offset estimates overlap within error for the low-angle North Lunggar detachment (minimum 8.1–12.8 km; maximum 15–20 km) and the Lamu Co strike-slip fault (12–22 km). Though the estimate for the North Lunggar rift based on thermal modeling is considered to be an absolute minimum, it is still within uncertainty of the displacement along the Lamu Co fault. Displacement rates between the North Lunggar rift and the Lamu Co fault are also similar, corroborating our interpretation of a kinematic linkage from geologic mapping (Figure 3b). The mean horizontal extension rate of the North Lunggar rift of 1.2–2.4 mm a^{-1} is equal within uncertainty and oriented subparallel to the geodetically determined interseismic slip rate for the Lamu Co fault of 1.4–3.3 mm a^{-1} [*Taylor and Peltzer*, 2006].

[52] The similar geologic and geodetic slip rates for the North Lunggar rift and Lamu Co strike-slip fault are consistent with a constrictional strain state and an east-west oriented least compressive stress (σ_3) (Figure 2). Extrapolating the geodetically determined slip rate for the Lamu Co fault back in time and using the magnitude of 17 ± 5 km of fault slip suggests that the initiation of the Lamu Co fault occurred between 15.7 and 3.6 Ma [*Taylor and Peltzer*, 2006]. *Taylor and Peltzer* [2006] suggest that slip rates were not constant for the Lamu Co fault but rather have accelerated in Plio-

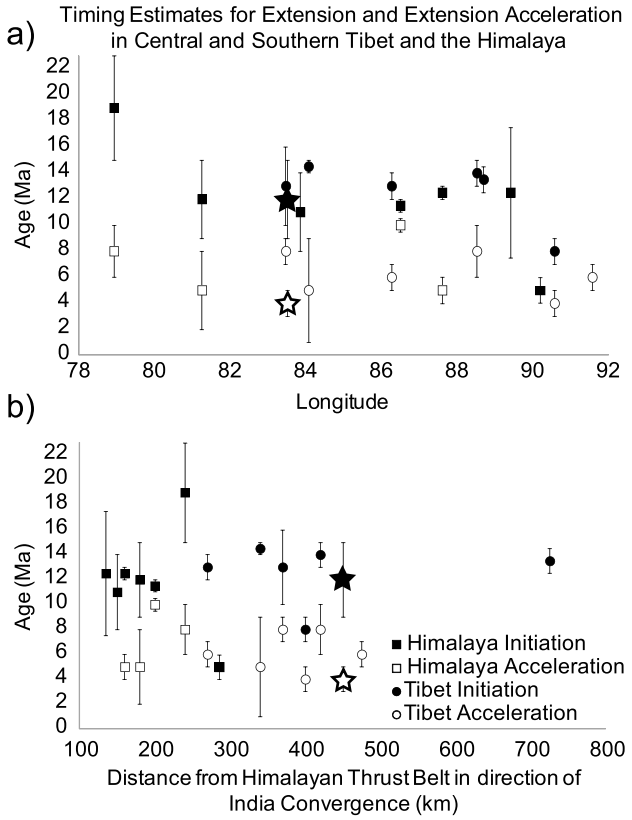

Figure 16. Timing estimates for extension initiation (black) and acceleration (white) of extension plotted against longitude for the Himalaya (squares) and central and southern Tibet (circles); stars represent estimates for the North Lunggar rift.

Pleistocene time, initiating along the BNS between 3 and 2 Ma based on structural reconstructions incorporating north-south contraction and east-west stretching rates. If correct, this may be evidence for acceleration in both rifting and kinematically linked strike-slip faulting (i.e., constriction) in Pliocene time, although in order to confidently make this claim a more detailed data set and more rigorous approach for comparing the geologic and geodetic rates within that data set is necessary [e.g., *Friedrich et al*., 2003].

[53] Results from the North Lunggar rift and Lamu Co fault, as well as other kinematically linked strike-slip and rift structures across southern Tibet, are consistent with plateau-wide observations for rate and the structural style of deformation. Geologic estimates suggest central Tibet has accommodated at least 30–60 km of east-west stretching since the middle Miocene, with <15 km of estimated north-south shortening since that time [*Taylor et al*., 2003]. Present-day north-south contraction rates are estimated to be as high as 5 ± 3 mm a^{-1} in the ~21° direction, parallel to the India-Asia convergence direction [*Zhang et al*., 2004]. Though Tibet undergoes significant internal shortening, the majority of shortening is accommodated along the plateau margins of the Himalaya, Altyn Tagh, and Qilian Shan-Nan Shan [*Zhang et al*., 2004]. East-west stretching rates within Tibet are approximately twice that of north-south contraction rates [*Zhang et al*., 2004]. The vertical strain field within the Tibetan plateau may also depend significantly on local elevation and relief, as the majority of active dip-slip structures are observed in areas with mean elevations exceeding 4500 m [*Molnar and Lyon-Caen*, 1989; *Kapp and Guynn*, 2004], meaning this may be a causal relationship between the style of faulting and elevation, with the state of stress being controlled by lateral variations in elevation and gravitational potential energy. Extension yields net thinning of the crust; however, there is an overall increase in elevation and gravitational potential energy from the BNS toward southern Tibet, thus making central Tibet more favorable for strike-slip faulting [*Mercier et al*., 1987; *Molnar and Lyon-Caen*, 1989]. This indicates σ_1 and σ_2 are similar in magnitude and that the boundary between the BNS and the Lhasa terrane may represent a gravitational potential energy threshold between which normal and strike-slip faults preferentially form. A change of the vertical principal stress from σ_1 to σ_2 while maintaining the same east-west orientation of σ_3 suggests the maximum principal stretching direction ($\hat{s}_1$) is oriented ~120°, consistent with constriction, as displayed at the local scale of the North Lunggar rift and Lamu Co fault systems (Figure 3b).

6.3. Relationship Between Extension and Magmatism

[54] Zircon U-Pb ages from plutonic rocks collected from the North Lunggar footwall yield two distinct age groups, one between 152 and 124 Ma and the other between 22 and 9 Ma. Samples from the northern and southern sections of the rift footwall yield apatite and zircon cooling ages similar to those located in the center of the footwall but with much older (Jurassic-Cretaceous) zircon U-Pb ages for those same northern and southern samples (Figures 4 and 7a). This suggests that magmatism at the northern and southern tips of the rift was unrelated to extensional footwall cooling. Conversely, Miocene zircon U-Pb ages from leucogranites in the central footwall as young as ~9 Ma suggest that granite emplacement likely took place during rifting (Figure 7a). Central footwall leucogranite samples with U-Pb zircon ages between 15 and 9 Ma are further evidence that Miocene magmatism in the North Lunggar footwall may have been coeval with early, slower stages of rifting.

[55] Tibetan rifts typically show evidence for synkinematic magmatic activity [e.g., *Harrison et al*., 1995], as do other areas undergoing large-magnitude extension such as in western North America [e.g., *McGrew et al*., 2000]. Leucogranite crystallization ages from the North Lunggar rift footwall are similar to other south Tibetan and Himalayan rifts such as Nyainqentanghla [*Harrison et al*., 1995; *J. Kapp et al*., 2005] and Gurla Mandhata [*Murphy et al*., 2002; A. T. McCallister et al., Thermochronologic constraints on the Late Cenozoic exhumation history of the Gurla Mandhata metamorphic core complex, Southwestern Tibet, *Tectonics*, in review 2013], which have abundant leucogranites in the 20–13 Ma age range. Leucogranite emplacement typically occurs during large-magnitude extension [e.g., *López-Moro et al*., 2012] and may correspond to the earliest stages of rift initiation. The influence of magmatism on the development of the North Lunggar rift as a whole is not completely clear. Melt weakening, while it is probably not the only mechanism, likely contributed to rift initiation. Some models suggest large-magnitude rift systems develop solely in response to thermal weakening and magmatic processes [e.g., *Lister and Baldwin*, 1993]. It is plausible that extension was in part triggered by magmatic activity, catalyzing rapid

Table 4. Timing Estimates for Extension Initiation and Secondary Stages of Rifting[a]

Rift	Distance From HTB (km)	Initiation Age (Ma)	± (Ma)	Second Stage (Ma)	± (Ma)	Reference(s)
			Central Tibet			
Shuang Hu	725	13.5	1.0			*Blisniuk et al*. [2001]
			Southern Tibet			
Gulu	475			6.0	1.0	*Stockli et al*. [2002]
LopuKangri	340	14.5	0.5	5.0	4.0	*Murphy et al*. [2010]; *Sanchez et al*. [2010]
North Lunggar	450	12.0	3.0	4.0	1.0	*Kapp et al*. [2008]; *Woodruff et al*. [2013] this study
Nyainqentanghla	400	8.0	1.0	4.0	1.0	*Harrison et al.* [1995]; *J. Kapp et al*. [2005].
Pum Qu-Xainza	420	14.0	1.0	8.0	2.0	*Hager et al*. [2009]
South Lunggar	370	13.0	3.0	8.0	1.0	*Styron et al*. [2013]
Tangra Yum Co	270	13.0	1.0	6.0	1.0	*Dewane et al*. [2006]
			Himalaya			
Ama Drime	160	12.5	0.5	5.0	1.0	*Kali et al*. [2010]
Gurla Mandhata	180	12.0	3.0	5.0	3.0	*Murphy et al*. [2002]; McCallister et al., submitted manuscript (2013)
Kung Co	200	11.5	0.5	10.0	0.5	*Lee et al*. [2011]
Leo Parghil	240	19.0	4.0	8.0	2.0	*Thiede et al*. [2006]; *Langille et al*. [2012]
Ringbung	285	5.0	1.0			*Ratschbacher et al*. [2011]
Thakkhola	150	11.0	3.0			*Coleman and Hodges* [1995]; *Garzione et al*. [2000]
Yadong	135	12.5	5.0			*Edwards and Harrison* [1997]

[a]HTB = Himalayan Thrust Belt.

uplift, or at least enhanced by thermal weakening [e.g., *Tirel et al*., 2008]; however, whether magmatism was a consequence of, facilitated, or initiated rifting altogether remains unclear.

6.4. Acceleration of Rifting in Tibet

[56] Rift acceleration in the Himalaya and Tibet has been documented [e.g., *Thiede et al*., 2006; *Lee et al*., 2011; *Styron et al*., 2013; this study], but few hypotheses have been proposed to explain the observation that many, but not all, large-magnitude rifts show later, accelerated exhumation many million years after rift inception. Strain rate variability may be driven by intrinsic (local), rift-specific changes in rheology and strain accumulation (i.e., strain hardening/softening, magmatism) or driven by extrinsic (regional) effects (i.e., gravitational potential energy, tectonic forces) as implied in many previously proposed models for syncollisional extension in the Himalaya and Tibet [e.g., *Dewey*, 1988; *Klootwijk et al*., 1985; *England and Houseman*, 1988; *Yin*, 2000].

[57] Acceleration of east-west extension may represent a common stage in the development of large-magnitude rifts in areas characterized by hot, thickened crust. The Himalaya and Tibet may be particularly susceptible to rift evolution involving highly variable extension rates due to its crustal thickness [*Holt and Wallace*, 1990] and high heat flow [*Francheteau et al*., 1984], as lithospheric strength is critically controlled by these factors with thicker, hotter crust being inherently weaker [*Kusznir and Park*, 1987]. Thermomechanical finite element modeling has shown that rheology may play a critical role in the deformation of the lithosphere, particularly in the development of focused shear zones, resulting in decreasing and increasing rift velocity [*Huismans and Beaumont*, 2003]. Strain localization can determine the style of lithospheric deformation in an extensional regime [*Frederiksen and Braun*, 2001], as changes to rheology alone can drive acceleration and deceleration of rifting in the presence of a constant extensional force [*Takeshita and Yamaji*, 1990]. Rheologic changes related to magmatic activity may also factor into deformation by promoting thermal weakening and strain localization in the crust [*Whitney et al*., 2013], thus facilitating extension via a feedback mechanism between magmatism and extension during decompression and crustal thinning [*Teyssier and Whitney*, 2002].

[58] Alternatively, acceleration of rifting may be primarily controlled by regional tectonic forces, specifically the convergence rate and northward extent of subducting Indian lithosphere. The collision of India with Asia played a major role in the thickening and Cenozoic construction of the Himalayan-Tibetan plateau [*Yin and Harrison*, 2000] and subsequent gravitational orogenic collapse resulting in the onset of extension observed in Miocene time [e.g., *Dewey*, 1988]; thus, it likely plays a critical role in determining the current tectonic regime. Rift acceleration may occur as the northern edge of the underthrusting Indian slab approaches the already active rift, forcing the weaker ductile material at depth toward the free boundary to the east, resulting in constriction and V-shaped conjugate strike-slip faults in the overlying central Tibetan lithosphere [*Yin and Taylor*, 2011]. Recent studies suggest that the position and northward extent of the obliquely underthrusting Indian slab may be located just south of the BNS between 31°N [*Nábělek et al*., 2009] and 31.5°N [*Mechie et al*., 2012] (Figure 1). This is consistent with timing estimates for rift acceleration in the Himalaya and Tibet which show, albeit sparsely, slightly younger timing for acceleration in the Lhasa terrane (8–4 Ma) compared to estimates in the Himalaya (10–5 Ma) (Figure 16; see Figure 1 for references) (Table 4). Though purely conjectural, as there are too few data points to draw any reliable trends across the Himalaya and Tibet, this south to north younging of rift acceleration at least provides a regional observation explaining the heterogeneity in extension rates observed.

[59] A third explanation is that the observation of rift acceleration is the result of a sampling bias toward the centers of the rifts where the most extension has taken place and that

the rates in the central parts of the rifts have slowed but the rift tips are actively experiencing rapid extension today. This implies that strain rates vary along strike, as well as through time, thus resulting in an extension rate that is constant through time but with strain accommodated in a heterogeneous manner along strike. This cannot be resolved using low-temperature thermochronology, because there has not been enough exhumation at the rift tips to record this exhumation history, and thus warrants further investigation.

[60] We speculate that a combination of the two former hypotheses explains acceleration of rifting in southern Tibet. In this view, rift initiation is caused by the regional stress state (i.e., excess gravitational potential energy). Large-magnitude rifts in some cases evolve into low-angle detachment systems resulting in domal footwalls (e.g., Nyainqentanghla), whereas other rifts appear to remain dominantly high-angle (e.g., Tangra Yum Co) but continuously stretch the upper crust hundreds of kilometers along strike and along variably segmented normal faults with each accommodating less slip. Rifting in either case localizes stretching of the upper middle crust, requires isostatic compensation of the middle crust, and, as rifting continues to develop, eventually results in compensation in the lower crust [e.g., *Block and Royden*, 1990; *Masek et al*., 1994]. Rift acceleration is a local response to regional tectonic forces, as isostatic compensation at depth is triggered first by ductile processes in the middle crust as India is underthrusting, causing a thermal perturbation of the inherently weaker [*Bird*, 1991] and rheologically more thermally sensitive lower crust or upper mantle [*Bürgmann and Dresen*, 2008]. Compensation in the lower crust results in rapid exhumation and extension observed in the upper crust a few million years after extension has already commenced. As low-angle underthrusting of India beneath Tibet continues northward, mantle-derived potassic volcanism ceases and is replaced by leucogranites derived from crustal melts. Deceleration may take place as the northern edge of the Indian slab passes by, continuing north of the previously accelerating rift segment, with strain localization resulting from increased magmatic activity [e.g., *Tirel et al*., 2008] or strain hardening/softening playing a lesser role in rift development [e.g., *Nielsen et al*., 2007]. Rifting in turn is more pronounced to the south in the Himalaya, as normal faulting is induced by the lateral spreading of the southern part of the plateau over the underthrusting Indian slab [*Armijo et al*., 1986; *DeCelles et al*., 2002].

7. Conclusions

[61] This study presents new apatite and zircon (U-Th)/He thermochronological data and zircon U-Pb geochronological data from the North Lunggar rift, west central southern Tibet. Our results and main conclusions are outlined below.

[62] 1. The North Lunggar rift exhumes an active extensional metamorphic core complex bounded by an east dipping low-angle normal fault. Thermochronology and thermal modeling document a minimum timing for rift initiation at >10 Ma and exhumation acceleration at 5–2 Ma. Miocene footwall cooling and exhumation rates were initially slow to moderate ($<50°C\,Ma^{-1}$ and $<1\,mm\,a^{-1}$), followed by Pliocene rift acceleration (up to $>400°C\,Ma^{-1}$ and $4–10\,mm\,a^{-1}$). The central section of the North Lunggar footwall underwent slightly more exhumation at higher rates than the northern and southern rift tips, resulting in rapid centralized extension and isostatic footwall rebound. Isothermal compression during rapid exhumation resulted in an elevated transient geothermal gradient between 50 and $90°C\,km^{-1}$.

[63] 2. The minimum magnitude of horizontal extension for the North Lunggar rift is 8.1–12.8 km with a minimum mean Pliocene rate of $1.2–2.4\,mm\,a^{-1}$ in the ~120° direction. This is similar in magnitude, rate, and orientation of slip to the kinematically linked Lamu Co dextral strike-slip fault to the north, which suggests a state of constrictional strain during Pliocene time in this part of Tibet. Results for this structural pair are consistent with plateau-wide observations for rate and the structural style of deformation which collectively suggest constriction along the BNS.

[64] 3. Jurassic-Cretaceous magmatism in the northern and southern North Lunggar footwall appears to be unrelated to Miocene-Pliocene extensional footwall cooling. Magmatism in the central section of the North Lunggar footwall was coeval with early stages of rift development where zircon U-Pb leucogranite ages (15–9 Ma) are consistent with the timing for onset of extension (>10 Ma). Whether magmatism facilitated the onset of extension or was the result of localized extension and decompression, or a combination of both, remains unclear.

[65] 4. Rift acceleration, as observed in the Himalaya and Tibet, remains a subject to be further explored due to the paucity of available timing constraints. A combination of rift-specific changes in rheology such as strain accumulation or magmatism driven primarily by regional tectonic forces potentially from the northward underthrusting of India may explain the apparent rift acceleration observed, as the Himalayan-Tibetan crust may be more susceptible to rifting with highly variable extension rates due to its hot, thickened crust.

[66] **Acknowledgments.** We thank Roman Kislitsyn and the Isotope Geochemistry Laboratory at the University of Kansas, Brain Horton, Brian Wernicke, and Will Woodruff for many insightful discussions during the 2009 field campaign, and Sarah Evans and Kyle Gorynski for discussions of HeMP modeling results and interpretations. We also thank Todd Ehlers (editor) and Lothar Ratschbacher (associate editor), as well as two anonymous reviewers who greatly improved the quality and clarity of this manuscript. Field work in Tibet would not have been possible without colleagues at the Institute of Tibetan Plateau Research, Chinese Academy of Sciences. This work was funded by the United States National Science Foundation Tectonics Grants EAR 0808976 and EAR 0911652. Support for the Arizona LaserChron Center was provided by NSF-EAR 1032156.

References

Abramowitz, M., and I. Stegun (1970), *Tables of Mathematical Functions*, National Bureau of Standards, Washington.

Allégre, C., V. Courtillot, P. Tapponnier, A. Hirn, M. Mattauer, C. Coulon, J. Jaeger, J. Achache, U. Schärer, and J. Marcoux (1984), Structure and evolution of the Himalaya-Tibet orogenic belt, *Nature*, *307*, 17–22, doi:10.1038/307017a0.

Armijo, R., P. Tapponnier, J. Mercier, and H. Tong-Lin (1986), Quaternary extension in southern Tibet: Field observations and tectonic implications, *J. Geophys. Res.*, *91*, 13,803–13,872, doi:10.1029/JB091iB14p13803.

Armijo, R., P. Tapponnier, and H. Tonglin (1989), Late Cenozoic dextral strike-slip faulting in southern Tibet, *J. Geophys. Res.*, *94*(B3), 2787–2838, doi:10.1029/JB094iB03p02787.

Axen, G. J., and J. M. Bartley (1997), Field tests of rolling hinges: Existence, mechanical types, and implications for extensional tectonics, *J. Geophys. Res.*, *102*(B9), 20,515–20,537, doi:10.1029/97JB01355.

Bird, P. (1991), Lateral extrusion of lower crust from under high topography in the isostatic limit, *J. Geophys. Res.*, *96*(B6), 10,275–10,286, doi:10.1029/91JB00370.

Blisniuk, P., B. Hacker, J. Glodny, L. Ratschbacher, S. Bi, Z. Wu, M. McWilliams, and A. Calvert (2001), Normal faulting in central Tibet since at least 13.5 Myr ago, *Nature*, *412*(6847), 628–632, doi:10.1038/35088045.

Block, L., and L. Royden (1990), Core complex geometries and regional scale flow in the lower crust, *Tectonics*, *9*(4), 557–567, doi:10.1029/TC009i004p00557.

Buck, W. (1988), Flexural rotation of normal faults, *Tectonics*, *7*(5), 959–973, doi:10.1029/TC007i005p00959.

Buck, W. (1991), Modes of continental lithospheric extension, *J. Geophys. Res.*, *96*(B12), 20,161–20,178, doi:10.1029/91JB01485.

Burchfiel, B. C., Z. Chen, L. H. Royden, Y. Liu, and C. Deng (1991), Extensional development of Gabo valley, southern Tibet, *Tectonophysics*, *194*(1), 187–193, doi:10.1016/0040-1951(91)90283-X.

Bürgmann, R., and G. Dresen (2008), Rheology of the lower crust and upper mantle: Evidence from rock mechanics, geodesy, and field observations, *Annu. Rev. Earth Planet. Sci.*, *36*, 531–567, doi:10.1146/annurev.earth.36.031207.124326.

Carslaw, H. S., and J. C. Jaeger (1959), *Conduction of Heat in Solids*, 2nd ed., 1 pp., Clarendon Press, Oxford.

Cheng, J., and G. Xu (1987), Geologic map of the Ritu region with report, Tibetan Bureau of Geological and Mineral Resources, 598.

Clark, M. K., and L. H. Royden (2000), Topographic ooze: Building the eastern margin of Tibet by lower crustal flow, *Geology*, *28*(8), 703–706.

Clark, M. K., K. A. Farley, D. Zheng, Z. Wang, and A. R. Duvall (2010), Early Cenozoic faulting of the northern Tibetan Plateau margin from apatite (U–Th)/He ages, *Earth Planet. Sci. Lett.*, *296*(1), 78–88.

Coleman, M., and K. Hodges (1995), Evidence for Tibetan plateau uplift before 14 Myr ago from a new minimum age for east–west extension, *Nature*, *374*(6517), 49–52, doi:10.1038/374049a0.

Coney, P., and T. Harms (1984), Cordilleran metamorphic core complexes: Cenozoic extensional relics of Mesozoic compression, *Geology*, *12*(9), 550–554.

Copley, A., J. P. Avouac, and B. P. Wernicke (2011), Evidence for mechanical coupling and strong Indian lower crust beneath southern Tibet, *Nature*, *472*(7341), 79–81, doi:10.1038/nature09926.

DeCelles, P. G., D. M. Robinson, and G. Zandt (2002), Implications of shortening in the Himalayan fold-thrust belt for uplift of the Tibetan Plateau, *Tectonics*, *21*(6), doi:10.1029/2001TC001322.

DeCelles, P., P. Kapp, J. Quade, and G. Gehrels (2011), Oligocene-Miocene Kailas basin, southwestern Tibet: Record of postcollisional upper-plate extension in the Indus-Yarlung suture zone, *Bull. Geol. Soc. Am.*, *123*(7–8), 1337–1362.

Dewane, T., D. Stockli, C. Hager, M. Taylor, L. Ding, J. Lee, and S. Wallis (2006), Timing of Cenozoic EW extension in the Tangra Yum Co-Kung Co rift, south-central Tibet, paper presented at American Geophysical Union, Fall Meeting (December 11–15, 2006), San Francisco.

Dewey, J. (1980), Episodicity, sequence and style at convergent plate boundaries, in The continental crust and its mineral deposits.

Dewey, J. (1988), Extensional collapse of orogens, *Tectonics*, 7(6), 1123–1139, doi:10.1029/TC007i006p01123.

Dewey, J., R. Shackleton, C. Chengfa, and S. Yiyin (1988), The tectonic evolution of the Tibetan Plateau, *Phil. Trans. Roy. Soc. Lond. Math Phys. Sci.*, *327*(1594), 379–413.

Ding, L., P. Kapp, D. Zhong, and W. Deng (2003), Cenozoic volcanism in Tibet: Evidence for a transition from oceanic to continental subduction, *J. Petrol.*, *44*(10), 1833–1865.

Edwards, M., and T. Harrison (1997), When did the roof collapse? Late Miocene north–south extension in the high Himalaya revealed by Th-Pb monazite dating of the Khula Kangri granite, *Geology*, *25*(6), 543–546.

Ehlers, T. A. (2005), Crustal thermal processes and the interpretation of thermochronometer data, *Rev. Mineral. Geochem.*, *58*(1), 315–350.

Ehlers, T., and K. Farley (2003), Apatite (U-Th)/He thermochronometry: Methods and applications to problems in tectonic and surface processes, *Earth Planet. Sci. Lett.*, *206*(1–2), 1–14.

Ehlers, T., P. Armstrong, and D. Chapman (2001), Normal fault thermal regimes and the interpretation of low-temperature thermochronometers, *Phys. Earth Planet. Inter.*, *126*(3), 179–194.

Ehlers, T. A., T. Chaudhri, S. Kumar, C. W. Fuller, S. D. Willett, R. A. Ketcham, M. T. Brandon, D. X. Belton, B. P. Kohn, and A. J. W. Gleadow (2005), Computational tools for low-temperature thermochronometer interpretation, *Rev. Mineral. Geochem.*, *58*(1), 589–622.

England, P. C., and G. A. Houseman (1988), The mechanics of the Tibetan Plateau, *Phil. Trans. Roy. Soc. Lond. Math Phys. Sci.*, *326*(1589), 301–320.

England, P., and G. Houseman (1989), Extension during continental convergence, with application to the Tibetan Plateau, *J. Geophys. Res.*, *94*, 17,561–17,579.

Farley, K. (2002), (U-Th)/He dating: Techniques, calibrations, and applications, *Rev. Mineral. Geochem.*, *47*(1), 819–844.

Farley, K., R. Wolf, and L. Silver (1996), The effects of long alpha-stopping distances on (U-Th)/He ages, *Geochim. Cosmochim. Acta*, *60*(21), 4223–4229.

Fielding, E., B. Isacks, M. Barazangi, and C. Duncan (1994), How flat is Tibet?, *Geology*, *22*(2), 163–167.

Fitzgerald, P. G., E. M. Duebendorfer, J. E. Faulds, and P. O'Sullivan (2009), South Virgin-White Hills detachment fault system of SE Nevada and NW Arizona: Applying apatite fission track thermochronology to constrain the tectonic evolution of a major continental detachment fault, *Tectonics*, *28*, doi:10.1029/2007TC002194.

Flowers, R., R. Ketcham, D. Shuster, and K. Farley (2009), Apatite (U-Th)/He thermochronometry using a radiation damage accumulation and annealing model, *Geochim. Cosmochim. Acta*, *73*(8), 2347–2365.

Francheteau, J., C. Jaupart, S. X. Jie, K. Wen-Hua, L. De-Lu, B. Jia-Chi, W. Hung-Pin, and D. Hsia-Yeu (1984), High heat flow in southern Tibet, *Nature*, *307*, 32–36.

Frederiksen, S., and J. Braun (2001), Numerical modelling of strain localisation during extension of the continental lithosphere, *Earth Planet. Sci. Lett.*, *188*(1), 241–251.

Friedrich, A. M., B. P. Wernicke, N. A. Niemi, R. A. Bennett, and J. L. Davis (2003), Comparison of geodetic and geologic data from the Wasatch region, Utah, and implications for the spectral character of Earth deformation at periods of 10 to 10 million years, *J. Geophys. Res.*, *108*(B4), 2199, doi:10.1029/2001JB000682.

Gao, Y., Z. Hou, B. S. Kamber, R. Wei, X. Meng, and R. Zhao (2007), Lamproitic rocks from a continental collision zone: Evidence for recycling of subducted Tethyan oceanic sediments in the mantle beneath southern Tibet, *J. Petrol.*, *48*(4), 729–752.

Garzanti, E., A. Baud, and G. Mascle (1987), Sedimentary record of the northward flight of India and its collision with Eurasia (Ladakh Himalaya, India), *Geodinamica Acta*, *1*(4–5), 297–312.

Garzione, C., D. Dettman, J. Quade, P. Decelles, and R. Butler (2000), High times on the Tibetan Plateau: Paleoelevation of the Thakkhola graben, Nepal, *Geology*, *28*(4), 339–342.

Gehrels, G. E., V. A. Valencia, and J. Ruiz (2008), Enhanced precision, accuracy, efficiency, and spatial resolution of U-Pb ages by laser ablation-multicollector-inductively coupled plasma-mass spectrometry, *Geochem. Geophys. Geosyst.*, *9*, Q03017, doi:10.1029/2007GC001805.

Girardeau, J., J. Marcoux, C. Allégre, J. Bassoullet, T. Youking, X. Xuchang, Z. Yougong, and W. Xibin (1984), Tectonic environment and geodynamic significance of the Neo-Cimmerian Donqiao ophiolite, Bangong-Nujiang suture zone, Tibet, *Nature*, *307*, 27–31.

Gottardi, R., C. Teyssier, A. Mulch, T. Vennemann, and M. Wells (2011), Preservation of an extreme transient geotherm in the Raft River detachment shear zone, *Geology*, *39*(8), 759–762.

Green, O. R., M. P. Searle, R. I. Corfield, and R. M. Corfield (2008), Cretaceous-Tertiary carbonate platform evolution and the age of the India-Asia collision along the Ladakh Himalaya (Northwest India), *J. Geol.*, *116*, 331–353.

Hager, C., and D. F. Stockli (2009), A new MATLAB©-based helium modeling package ("HeMP") for thermal history recovery from single and multi-thermochronometer (U-Th)/He data and data arrays, paper presented at GSA Annual Meeting (18–21 October 2009), Portland.

Hager, C., D. Stockli, T. Dewane, G. Gehrels, and L. Ding (2009), Anatomy and crustal evolution of the central Lhasa terrane (S-Tibet) revealed by investigations in the Xainza rift, paper presented in EGU General Assembly Conference Abstracts, vol. 11, p. 11346, (April 19–24), Vienna.

Harrison, T., and P. Zeitler (2005), Fundamentals of noble gas thermochronometry, *Rev. Mineral. Geochem.*, *58*(1), 123–149.

Harrison, T., P. Copeland, W. Kidd, and O. Lovera (1995), Activation of the Nyainqentanghla shear zone: Implications for uplift of the southern Tibetan Plateau, *Tectonics*, *14*(3), 658–676, doi:10.1029/95TC00608.

Hollingsworth, J., B. Wernicke, and L. Ding (2010), Fault slip-rate estimate for the dextral Beng Co strike-slip fault, based on Quaternary dating of displaced paleo-lake shorelines, paper presented at AGU Fall Meeting (December 13–17), vol. 1, p. 2229, San Francisco.

Holt, W. E., and T. C. Wallace (1990), Crustal thickness and upper mantle velocities in the Tibetan plateau region from the inversion of regional Pnl waveforms: Evidence for a thick upper mantle lid beneath southern Tibet, *J. Geophys. Res.*, *95*, 12,499–12,525, doi:10.1029/JB095iB08p12499.

Hourigan, J. K., P. W. Reiners, and M. T. Brandon (2005), U-Th zonation-dependent alpha-ejection in (U-Th)/He chronometry, *Geochim. Cosmochim. Acta*, *69*(13), 3349–3365.

Huang, W., J. Ni, F. Tilmann, D. Nelson, J. Guo, W. Zhao, J. Mechie, R. Kind, J. Saul, and R. Rapine (2000), Seismic polarization anisotropy beneath the central Tibetan Plateau, *J. Geophys. Res.*, *105*(B12), 27,979–27,989, doi:10.1029/2000JB900339.

Hubbard, M. S., and T. M. Harrison (1989), $^{40}Ar/^{39}Ar$ age constraints on deformation and metamorphism in the Main Central Thrust zone and Tibetan

Slab, eastern Nepal Himalaya, *Tectonics*, *8*(4), 865–880, doi:10.1029/TC008i004p00865.

Huismans, R. S., and C. Beaumont (2003), Symmetric and asymmetric lithospheric extension: Relative effects of frictional-plastic and viscous strain softening, *J. Geophys. Res. 108*(B10), 2496, doi:10.1029/2002JB002026.

Kali, E., P. Leloup, N. Arnaud, G. Mahéo, D. Liu, E. Boutonnet, J. Van der Woerd, X. Liu, J. Liu-Zeng, and H. Li (2010), Exhumation history of the deepest central Himalayan rocks, Ama Drime range: Key pressure-temperature-deformation-time constraints on orogenic models, *Tectonics*, *29*, TC2014, doi:10.1029/2009TC002551.

Kapp, P., and J. H. Guynn (2004), Indian punch rifts Tibet, *Geology*, *32*(11), 993–996.

Kapp, P., A. Yin, C. E. Manning, T. M. Harrison, M. H. Taylor, and L. Ding (2003), Tectonic evolution of the early Mesozoic blueschist-bearing Qiangtang metamorphic belt, central Tibet, *Tectonics*, *22*(4), 1043, doi:10.1029/2002TC001383.

Kapp, P., A. Yin, T. M. Harrison, and L. Ding (2005), Cretaceous-Tertiary shortening, basin development, and volcanism in central Tibet, *Geol. Soc. Am. Bull.*, *117*(7–8), 865–878.

Kapp, J. L. D., T. M. Harrison, P. Kapp, M. Grove, O. M. Lovera, and D. Lin (2005), Nyainqentanglha Shan: A window into the tectonic, thermal, and geochemical evolution of the Lhasa block, southern Tibet, *J. Geophys. Res.*, *110*, B08413, doi:10.1029/2004JB003330.

Kapp, P., P. G. DeCelles, G. E. Gehrels, M. Heizler, and L. Ding (2007), Geological records of the Lhasa-Qiangtang and Indo-Asian collisions in the Nima area of central Tibet, *Geol. Soc. Am. Bull.*, *119*(7–8), 917–932.

Kapp, P., M. Taylor, D. Stockli, and L. Ding (2008), Development of active low-angle normal fault systems during orogenic collapse: Insight from Tibet, *Geology*, *36*, 7–10.

Ketcham, R. (1996), Thermal models of core-complex evolution in Arizona and New Guinea: Implications for ancient cooling paths and present-day heat flow, *Tectonics*, *15*(5), 933–953, doi:10.1029/96TC00033.

Ketcham, R. A. (2005), Forward and inverse modeling of low-temperature thermochronometry data, *Rev. Mineral. Geochem.*, *58*(1), 275–314.

Ketcham, R. A., R. A. Donelick, and M. B. Donelick (2000), AFTSolve: A program for multi-kinetic modeling of apatite fission-track data, *Geol. Mater. Res.*, *2*(1), 1–32.

Klootwijk, C., P. Conaghan, and C. Powell (1985), The Himalayan Arc: Large-scale continental subduction, oroclinal bending and back-arc spreading, *Earth Planet. Sci. Lett.*, *75*(2–3), 167–183.

Kusznir, N. J., and R. G. Park (1987), The extensional strength of the continental lithosphere: Its dependence on geothermal gradient, and crustal composition and thickness, *Geol. Soc. Lond. Spec. Publ.*, *28*(1), 35–52.

Langille, J. M., M. J. Jessup, J. M. Cottle, G. Lederer, and T. Ahmad (2012), Timing of metamorphism, melting and exhumation of the Leo Pargil dome, northwest India, *J. Metamorphic Geol.*, *30*, 769–791, doi:10.1111/j.525-1314.2012.00998.x.

Lee, J., C. Hager, S. R. Wallis, D. F. Stockli, M. J. Whitehouse, M. Aoya, and Y. Wang (2011), Middle to late Miocene extremely rapid exhumation and thermal reequilibration in the Kung Co rift, southern Tibet, *Tectonics*, *30*(2), TC2007, doi:10.1029/2010TC002745.

Li, D., and A. Yin (2008), Orogen-parallel, active left-slip faults in the Eastern Himalaya: Implications for the growth mechanism of the Himalayan Arc, *Earth Planet. Sci. Lett.*, *274*(1–2), 258–267.

Lister, G. S., and S. L. Baldwin (1993), Plutonism and the origin of metamorphic core complexes, *Geology*, *21*(7), 607–610.

Lister, G., and G. Davis (1989), The origin of metamorphic core complexes and detachment faults formed during Tertiary continental extension in the northern Colorado River region, USA, *J. Struct. Geol.*, *11*(1–2), 65–94.

Liu, M., and Y. Yang (2003), Extensional collapse of the Tibetan Plateau: Results of three-dimensional finite element modeling, *J. Geophys. Res.*, *108*(8), 1–15, doi:10.1029/2002JB002248.

López-Moro, F. J., M. López-Plaza, and R. L. Romer (2012), Generation and emplacement of shear-related highly mobile crustal melts: The synkinematic leucogranites from the Variscan Tormes Dome, Western Spain, *Int. J. Earth Sci.*, 1–26.

Mahéo, G., P. Leloup, F. Valli, R. Lacassin, N. Arnaud, J. Paquette, A. Fernandez, L. Haibing, K. Farley, and P. Tapponnier (2007), Post 4 Ma initiation of normal faulting in southern Tibet. Constraints from the Kung Co half graben, *Earth Planet. Sci. Lett.*, *256*(1–2), 233–243.

Mancktelow, N. S., and B. Grasemann (1997), Time-dependent effects of heat advection and topography on cooling histories during erosion, *Tectonophysics*, *270*(3), 167–195.

Masek, J. G., B. L. Isacks, E. J. Fielding, and J. Browaeys (1994), Rift flank uplift in Tibet—Evidence for a viscous lower crust, *Tectonics*, *13*(3), 659–667, doi:10.1029/94TC00452.

McGrew, A. J., M. T. Peters, and J. E. Wright (2000), Thermobarometric constraints on the tectonothermal evolution of the East Humboldt Range metamorphic core complex, Nevada, *Geol. Soc. Am. Bull.*, *112*(1), 45–60.

Mechie, J., X. Yuan, B. Schurr, F. Schneider, C. Sippl, L. Ratschbacher, V. Minaev et al. (2012), Crustal and uppermost mantle velocity structure along a profile across the Pamir and southern Tien Shan as derived from project TIPAGE wide-angle seismic data, *Geophys. J. Int.*, *188*, 385–407, doi:10.1111/j.1365-246X.2011.05278.x.

Mercier, J., R. Armijo, P. Tapponnier, E. Carey-Gailhardis, and H. Lin (1987), Change from late Tertiary compression to Quaternary extension in southern Tibet during the India-Asia collision, *Tectonics*, *6*, 275–304, doi:10.1029/TC006i003p00275.

Molnar, P., and H. Lyon-Caen (1989), Fault plane solutions of earthquakes and active tectonics of the northern and eastern parts of the Tibetan Plateau, *Geophys. J. Int*, *99*, 123–153.

Molnar, P., and P. Tapponnier (1975), Cenozoic tectonics of Asia: Effects of a continental collision, *Science*, *189*(4201), 419–426.

Molnar, P., and P. Tapponnier (1978), Active tectonics of Tibet, *J. Geophys. Res.*, *83*(B11), 5361–5375.

Monastero, F. C., A. M. Katzenstein, J. S. Miller, J. R. Unruh, M. C. Adams, and K. Richards-Dinger (2005), The Coso geothermal field: A nascent metamorphic core complex, *Geol. Soc. Am. Bull.*, *117*(11–12), 1534–1553.

Monigle, P. W., J. Nábělek, J. Braunmiller, and N. S. Carpenter (2012), Evidence for low-angle normal faulting in the Pumqu-Xianza Rift, Tibet, *Geophys. J. Int.*, *190*, 1335–1340, doi:10.1111/j.1365-246X.2012.05581.x.

Murphy, M. A., and P. Copeland (2005), Transtensional deformation in the central Himalaya and its role in accommodating growth of the Himalayan orogen, *Tectonics*, *24*(4), TC4012, doi:10.1029/2004TC001659.

Murphy, M., A. Yin, P. Kapp, T. Harrison, C. Manning, F. Ryerson, D. Lin, and G. Jinghui (2002), Structural evolution of the Gurla Mandhata detachment system, southwest Tibet: Implications for the eastward extent of the Karakoram fault system, *Geol. Soc. Am. Bull.*, *114*(4), 428–447.

Murphy, M. A., V. Sanchez, and M. H. Taylor (2010), Syncollisional extension along the India–Asia suture zone, south-central Tibet: Implications for crustal deformation of Tibet, *Earth Planet. Sci. Lett.*, *290*(3), 233–243.

Nábělek, J., G. Hetényi, J. Vergne, S. Sapkota, B. Kafle, M. Jiang, H. Su, J. Chen, and B. S. Huang (2009), Underplating in the Himalaya-Tibet collision zone revealed by the Hi-CLIMB experiment, *Science*, *325*(5946), 1371–1374.

Nelson, K. D., W. Zhao, L. Brown, J. Kuo, J. Che, X. Liu, S. Klemperer, Y. Makovsky, R. Meissner, and J. Mechie (1996), Partially molten middle crust beneath southern Tibet: Synthesis of project INDEPTH results, *Science*, *274*(5293), 1684–1688.

Nielsen, S. B., R. Stephenson, and E. Thomsen (2007), Dynamics of Mid-Palaeocene North Atlantic rifting linked with European intra-plate deformations, *Nature*, *450*(7172), 1071–1074.

Pan, Y., and W. S. F. Kidd (1992), Nyainqentanghla shear zone—A late Miocene extensional detachment in the southern Tibetan Plateau, *Geology*, *20*(9), 775–778.

Powell, W. G., D. S. Chapman, N. Balling, and A. E. Beck (1988), Continental heat-flow density, Handbook of Terrestrial Heat-Flow Density Determination, 167–222.

Ratschbacher, L., I. Krumrei, M. Blumenwitz, M. Staiger, R. Gloaguen, B. V. Miller, S. D. Samson, M. A. Edwards, and E. Appel (2011), Rifting and strike-slip shear in central Tibet and the geometry, age and kinematics of upper crustal extension in Tibet, *Geol. Soc. Lond. Spec. Publ.*, *353*(1), 127–163.

Regenauer-Lieb, K., R. F. Weinberg, and G. Rosenbaum (2006), The effect of energy feedbacks on continental strength, *Nature*, *442*(7098), 67–70, doi:10.1038/nature04868.

Reiners, P. (2005), Zircon (U-Th)/He thermochronometry, *Rev. Mineral. Geochem.*, *58*(1), 151–179.

Reiners, P. W., R. Brady, K. A. Farley, J. E. Fryxell, B. Wernicke, and D. Lux (2000), Helium Earth and Planetary Science Letters, 178(3–4), 315–326.

Reiners, P., T. Spell, S. Nicolescu, and K. Zanetti (2004), Zircon (U-Th)/He thermochronometry: He diffusion and comparisons with 40Ar/39Ar dating, *Geochimica Et Cosmochimica Acta*, *68*(8), 1857–1887.

Rohrmann, A., P. Kapp, B. Carrapa, P. W. Reiners, J. Guynn, L. Ding, and M. Heizler (2012), Thermochronologic evidence for plateau formation in central Tibet by 45 Ma, *Geology*, *40*, 187–190.

Royden, L. (1996), Coupling and decoupling of crust and mantle in convergent orogens: Implications for strain partitioning in the crust, *J. Geophys. Res.*, *101*(B8), 17,679–17,706.

Royden, L., B. Burchfiel, R. King, E. Wang, Z. Chen, F. Shen, and Y. Liu (1997), Surface deformation and lower crustal flow in eastern Tibet, *Science*, *276*(5313), 788–790.

Sanchez, V., M. Murphy, A. Robinson, T. Lapen, M. Heizler, and M. Taylor (2010), Onset of oblique extension in south-central Tibet by 15 Ma: Implications for diachronous extension of the Tibetan Plateau, paper presented in AGU Fall Meeting Abstracts (December 13–17), San Francisco.

Schill, E., E. Appel, O. Zeh, V. Singh, and P. Gautam (2001), Coupling of late-orogenic tectonics and secondary pyrrhotite remanences: Towards a separation of different rotation processes and quantification of rotational underthrusting in the western Himalaya (northern India), *Tectonophysics*, *337*(1–2), 1–21.

Shuster, D. L., R. M. Flowers, and K. A. Farley (2006), The influence of natural radiation damage on helium diffusion kinetics in apatite, *Earth Planet. Sci. Lett.*, *249*(3–4), 148–161.

Spencer, J. (1984), Role of tectonic denudation in warping and uplift of low-angle normal faults, *Geology*, *12*(2), 95–98.

Stockli, D. F. (2005), Application of low-temperature thermochronometry to extensional tectonic settings, *Rev. Mineral. Geochem.*, *58*(1), 411–448.

Stockli, D. F., K. A. Farley, and T. A. Dumitru (2000), Calibration of the apatite (U-Th)/He thermochronometer on an exhumed fault block, White Mountains, California, *Geology*, *28*(11), 983–986.

Stockli, D., M. Taylor, A. Yin, T. Harrison, J. D'Andrea, P. Kapp, and L. Ding (2002a), Late Miocene–Pliocene inception of EW extension in Tibet as evidenced by apatite (U-Th), He data: Geological Society of America Abstracts with Programs (October 27–30), Denver, 34(6), 411.

Stockli, D. F., B. E. Surpless, T. A. Dumitru, and K. A. Farley (2002b), Thermochronological constraints on the timing and magnitude of Miocene and Pliocene extension in the central Wassuk Range, western Nevada, *Tectonics*, *21*(4), 1028, doi:10.1029/2001TC001295.

Stockli, D. F., T. A. Dumitru, M. O. McWilliams, and K. A. Farley (2003), Cenozoic tectonic evolution of the White Mountains, California and Nevada, *Geol. Soc. Am. Bull.*, *115*(7), 788–816.

Styron, R., M. Taylor, and K. Okoronkwo (2010), Database of active structures from the Indo-Asian collision, *EOS Transactions*, *91*, 181–182.

Styron, R., M. Taylor, K. E. Sundell, D. F. Stockli, J. A. G. Oalmann, A. Möller, A. T. McCallister, D. Liu, and L. Ding (2013), Miocene initiation and acceleration of extension in the South Lunggar rift, western Tibet: Evolution of an active detachment system from structural mapping and (U-Th)/He thermochronology, *Tectonics*, *32*, 1–28, doi:10.1002/tect.20053.

Takeshita, T., and A. Yamaji (1990), Acceleration of continental rifting due to a thermomechanical instability, *Tectonophysics*, *181*(1), 307–320.

Taylor, M., and G. Peltzer (2006), Current slip rates on conjugate strike-slip faults in central Tibet using synthetic aperture radar interferometry, *J. Geophys. Res.*, *111*, B12402, doi:10.1029/2005JB004014.

Taylor, M., and A. Yin (2009), Active structures of the Himalayan-Tibetan orogen and their relationships to earthquake distribution, contemporary strain field, and Cenozoic volcanism, *Geosphere*, *5*(3), 199–214.

Taylor, M., A. Yin, F. Ryerson, P. Kapp, and L. Ding (2003), Conjugate strike-slip faulting along the Bangong-Nujiang suture zone accommodates coeval east–west extension and north–south shortening in the interior of the Tibetan Plateau, *Tectonics*, *22*(4), 1044, doi: 10.1029/2002TC001361.

Teyssier, C., and D. L. Whitney (2002), Gneiss domes and orogeny, *Geology*, *30*(12), 1139–1142.

Thiede, R., J. Arrowsmith, B. Bookhagen, M. McWilliams, E. Sobel, and M. Strecker (2006), Dome formation and extension in the Tethyan Himalaya, Leo Pargil, northwest India, *Bull. Geol. Soc. Am.*, *118*(5–6), 635–650.

Tirel, C., J. P. Brun, and E. Burov (2008), Dynamics and structural development of metamorphic core complexes, *J. Geophys. Res.*, *113*, B04403, doi:10.1029/2005JB003694.

Tucholke, B. E., J. Lin, and M. C. Kleinrock (1998), Megamullions and mullion structure defining oceanic metamorphic core complexes on the Mid-Atlantic Ridge, *J. Geophys. Res.*, *103*(B5), 9857–9866.

Twiss, R., and E. Moores (2007), *Structural Geology*, 736 pp., WH Freeman and Company, New York.

van Hinsbergen, D. J. J., B. Steinberger, P. V. Doubrovine, and R. Gassmoller (2011), Acceleration and deceleration of India-Asia convergence since the Cretaceous: Roles of mantle plumes and continental collision, *J. Geophys. Res.*, *116*, B06101, doi:10.1029/2010JB008051.

Vermeesch, P., D. Seward, C. Latkoczy, M. Wipf, D. Günther, and H. Baur (2007), α-Emitting mineral inclusions in apatite, their effect on (U–Th)/He ages, and how to reduce it, *Geochim. Cosmochim. Acta*, *71*(7), 1737–1746.

Wang, J., X. Hu, L. Jansa, and Z. Huang (2011), Provenance of the Upper Cretaceous–Eocene deep-water sandstones in Sangdanlin, southern Tibet: Constraints on the timing of initial India-Asia collision, *J. Geol.*, *119*(3), 293–309.

Wernicke, B., and G. Axen (1988), On the role of isostasy in the evolution of normal fault systems, *Geology*, *16*(9), 848–851.

Whitney, D. L., C. Teyssier, P. Rey, and W. R. Buck (2013), Continental and oceanic core complexes, *Geol. Soc. Am. Bull.*, doi:10.1130/B30754.1.

Whittington, A. G., A. M. Hofmeister, and P. I. Nábělek (2009), Temperature-dependent thermal diffusivity of the Earth's crust and implications for magmatism, *Nature*, *458*(7236), 319–321.

Williams, H., S. Turner, S. Kelley, and N. Harris (2001), Age and composition of dikes in Southern Tibet: New constraints on the timing of east–west extension and its relationship to postcollisional volcanism, *Geology*, *29*(4), 339–342.

Wolf, R. A., K. A. Farley, and L. T. Silver (1996), Helium diffusion and low-temperature thermochronometry of apatite, *Geochimica Et Cosmochimica Acta*, *60*(21), 4231–4240.

Wolf, R. A., K. A. Farley, and D. M. Kass (1998), Modeling of the temperature sensitivity of the apatite (U-Th)/He thermochronometer, *Chem. Geol.*, *148*(1–2), 105–114.

Wolfe, M. R., and D. F. Stockli (2010), Zircon (U-Th)/He thermochronometry in the KTB drill hole, Germany, and its implications for bulk He diffusion kinetics in zircon, *Earth Planet. Sci. Lett.*, *295*(1–2), 69–82.

Woodruff, W. H., B. K. Horton, P. Kapp, and D. F. Stockli (2013), Late Cenozoic evolution of the Lunggar extensional basin, Tibet: Implications for basin growth and exhumation in hinterland plateaus, *Geol. Soc. Am. Bull.*, *125*, 343–358.

Yin, A. (2000), Mode of Cenozoic east–west extension in Tibet suggesting a common origin of rifts in Asia during the Indo-Asian collision, *J. Geophys. Res.*, *105*(B9), 21,745–721,759, doi:10.1029/2000JB900168.

Yin, A. (2010), Cenozoic tectonic evolution of Asia: A preliminary synthesis, *Tectonophysics*, *488*(1), 293–325.

Yin, A., and T. M. Harrison (2000), Geologic evolution of the Himalayan-Tibetan orogen, *Annu. Rev. Earth Planet. Sci.*, *28*, 211–280.

Yin, A., and M. H. Taylor (2011), Mechanics of V-shaped conjugate strike-slip faults and the corresponding continuum mode of continental deformation, *Geol. Soc. Am. Bull.*, *123*(9–10), 1798–1821.

Yin, A., T. M. Harrison, F. Ryerson, W. Chen, W. Kidd, and P. Copeland (1994), Tertiary structural evolution of the Gangdese thrust system, southeastern Tibet, *J. Geophys. Res.*, *99*(18), 175–118.

Zhang, P. Z., Z. Shen, M. Wang, W. J. Gan, R. Bürgmann, and P. Molnar (2004), Continuous deformation of the Tibetan Plateau from global positioning system data, *Geology*, *32*(9), 809–812.

Zhang, H., N. Harris, R. Parrish, S. Kelley, L. Zhang, N. Rogers, T. Argles, and J. King (2004), Causes and consequences of protracted melting of the mid-crust exposed in the North Himalayan antiform, *Earth Planet. Sci. Lett.*, *228*(1), 195–212.

Zhu, B., W. S. F. Kidd, D. B. Rowley, B. S. Currie, and N. Shafique (2005), Age of initiation of the India-Asia collision in the east-central Himalaya, *J. Geol.*, *113*, 265–285.

Zhu, D.-C., Z.-D. Zhao, Y. Niu, X.-X. Mo, S.-L. Chung, Z.-Q. Hou, L.-Q. Wang, and F.-Y. Wu (2011), The Lhasa Terrane: Record of a microcontinent and its histories of drift and growth, *Earth Planet. Sci. Lett.*, *301*, 241–255.